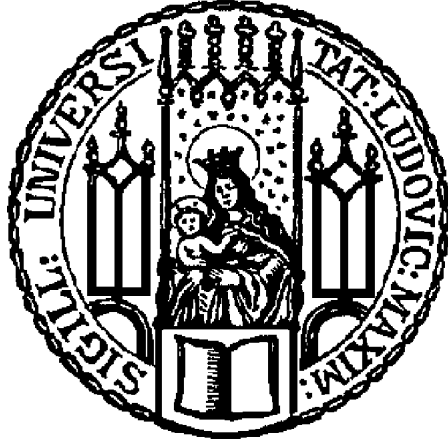


# Electron Identification in Dilepton Searches for Supersymmetry



Diplomarbeit der Fakultät für Physik  
der  
Ludwig-Maximilians-Universität München

vorgelegt von

**Josipa Vujaklija**

geboren in Slavonski Brod, Kroatien

---

München, den 19.07.2011



Erstgutachterin:  
Zweitgutachter:

Prof. Dr. Dorothee Schaile  
Prof. Dr. Jochen Schieck



## Abstract

The Large Hadron Collider (LHC) at CERN, which runs since 2010 at a centre-of-mass energy of 7 TeV, offers a huge potential for shedding light on fundamental open questions within the field of particle physics. It aims at finding the still undetected Higgs boson and to look for new physics beyond the Standard Model.

Supersymmetry (SUSY) is a symmetry that relates fermions and bosons and constitutes a promising candidate in the search for new physics at the weak scale. The existence of SUSY is still unproven, yet a large number of supersymmetric scenarios providing each different signatures, exist.

They may be studied with ATLAS, a general purpose detector at CERN. R-parity conserving SUSY searches at ATLAS are split into channels involving different numbers of isolated final state leptons.

In the dilepton channel two isolated leptons (electrons or muons), high-energetic jets as well as high Missing Transverse Energy are required. The challenge is to disentangle possibly present SUSY signal from ordinary Standard Model background.

In this thesis, the QCD background coming from multi-jet production and present in the dielectron signal regions, is studied using a data-driven estimation technique. Jets that have been reconstructed as leptons due to mismeasurement in the detector, are referred to as fake leptons. Real leptons come from electroweak processes. The probability that a reconstructed electron is fake or real can be measured using control regions rich in fake or real electrons. Using the measured efficiency and fake rate, an estimation of the QCD background is given.



## Zusammenfassung

Der Large Hadron Collider (LHC) am CERN, der seit 2010 bei einer Schwerpunktsenergie von 7 TeV im Betrieb ist, birgt großes Potential, um Licht auf noch offene fundamentale Fragen der Teilchenphysik zu werfen. Sein Ziel ist es, das noch nicht nachgewiesene Higgs Boson zu finden, sowie neue Physik jenseits des Standardmodells zu erforschen.

Supersymmetrie (SUSY) ist eine Symmetrie, die Fermionen mit Bosonen verknüpft und einen vielversprechenden Kandidaten bei der Suche nach neuer Physik bei Energien der schwachen Skala darstellt. Die Existenz von SUSY ist noch nicht gesichert, jedoch existiert eine große Anzahl denkbarer supersymmetrischer Szenarien, die alle durch eine bestimmte Signatur gekennzeichnet sind.

Diese können mit dem ATLAS Detektor, einem Universaldetektor am CERN, genauer untersucht werden. R-Parität erhaltende SUSY-Suchen bei ATLAS sind in verschiedene Kanäle unterteilt, die sich in der Anzahl der isolierten Leptonen im Endzustand unterscheiden.

Der 2-Lepton Kanal fordert zwei isolierte Leptonen (Elektronen oder Muonen), hochenergetische Jets, sowie eine hohe fehlende transversale Energie. Die Herausforderung hierbei ist es, womöglich vorhandene SUSY Signale von gewöhnlichen Untergrundprozessen des Standardmodells trennen zu können.

In der vorliegenden Arbeit wird der QCD Untergrund, der von Multijet-Ereignissen stammt und in den Signalregionen mit zwei Elektronen im Endzustand vorhanden ist, mit einer datengestützten Methode genauer untersucht.

Als sogenannte “fake” Leptonen werden Jets bezeichnet, die aufgrund einer Fehlmessung im Detektor als Leptonen rekonstruiert wurden. “Real” Leptonen stammen hingegen von elektroschwachen Prozessen. Die Wahrscheinlichkeit, dass ein rekonstruiertes Elektron einen fake oder real Ursprung hat, kann mit Hilfe verschiedener Kontrollregionen berechnet werden. Diese enthalten entweder viele fake Elektronen oder viele real Elektronen.

Unter Verwendung von real-Effizienzen und fake-Raten wird eine Abschätzung des QCD Untergrundes abgeleitet.





# Contents

<b>1</b>	<b>Introduction</b>	<b>1</b>
1.1	Standard Model of Particle Physics . . . . .	1
1.1.1	Overview . . . . .	1
1.1.2	Strong Interaction . . . . .	2
1.1.3	Electroweak Theory and Symmetry Breaking . . . . .	3
1.2	Open Issues Concerning the Standard Model . . . . .	4
1.3	Supersymmetry as a Possible Extension of the Standard Model . . . . .	5
1.3.1	SUSY - A Symmetry between Fermions and Bosons . . . . .	5
1.3.2	Field Content of the MSSM . . . . .	6
1.3.3	Supersymmetry Breaking . . . . .	7
<b>2</b>	<b>LHC and the ATLAS Experiment at CERN</b>	<b>9</b>
2.1	The LHC . . . . .	9
2.2	The ATLAS Detector . . . . .	12
2.2.1	Coordinate System . . . . .	13
2.2.2	Components of the ATLAS Detector . . . . .	13
2.2.2.1	Inner Detector . . . . .	14
2.2.2.2	Calorimeter . . . . .	14
2.2.2.3	Muon Detector . . . . .	15
2.2.2.4	Magnet System . . . . .	16
2.2.2.5	Trigger Architecture . . . . .	16
2.2.3	The LHC Computing Grid . . . . .	17
<b>3</b>	<b>SUSY Searches at ATLAS in the Dilepton Channel</b>	<b>19</b>
3.1	Introduction . . . . .	19
3.2	The Dilepton Channel . . . . .	19
3.3	Important Backgrounds to Dilepton Searches . . . . .	22
3.4	Object Reconstruction and Identification . . . . .	23
3.4.1	Electrons . . . . .	23
3.4.1.1	Reconstruction . . . . .	23
3.4.1.2	Identification . . . . .	23
3.4.2	Muons . . . . .	24
3.4.3	Jets . . . . .	24
<b>4</b>	<b>Object and Event Selection in the 2011 Analysis</b>	<b>25</b>
4.1	Event Selection I . . . . .	25
4.2	Object Definitions and Overlap Removal . . . . .	25
4.2.1	Electrons . . . . .	26
4.2.2	Muons . . . . .	26

4.2.3	Jets . . . . .	26
4.3	Event Selection II . . . . .	27
4.3.1	PileupReweighting . . . . .	27
4.3.2	Calculation of Missing Transverse Energy . . . . .	28
4.3.3	Signal Regions . . . . .	28
4.4	Monte Carlo and Data Samples . . . . .	29
4.5	Monte Carlo and Data Comparison . . . . .	29
4.5.1	Dielectron OS Channel . . . . .	30
4.5.2	Dielectron SS Channel . . . . .	31
<b>5</b>	<b>QCD Background Estimation Using the Matrix Method</b>	<b>33</b>
5.1	Matrix Method . . . . .	33
5.1.1	Single-Lepton Channel . . . . .	34
5.1.2	Dilepton Channel . . . . .	34
<b>6</b>	<b>QCD Background Estimation with 2011 Data</b>	<b>37</b>
6.1	Loose / Tight Definitions for Electrons . . . . .	37
6.2	Choice of Control Regions . . . . .	37
6.3	Real Electron Control Region . . . . .	40
6.4	Fake Control Region . . . . .	40
6.5	Real Efficiencies . . . . .	41
6.6	Fake Rates . . . . .	42
6.7	Results . . . . .	43
6.7.1	OS Signal Region - 1 . . . . .	43
6.7.2	OS Signal Region - 2 . . . . .	45
6.7.3	OS Signal Region - 3 . . . . .	46
6.7.4	SS Signal Region - 1 . . . . .	48
6.7.5	SS Signal Region - 2 . . . . .	49
6.8	Discussion . . . . .	51
<b>7</b>	<b>Summary</b>	<b>53</b>
<b>A</b>	<b>Results from QCD Background Estimation with 2010 Data</b>	<b>55</b>
A.1	Real Efficiencies . . . . .	56
A.2	Fake Rates . . . . .	57
A.3	Results . . . . .	58
A.3.1	OS SR . . . . .	58
A.3.2	SS SR . . . . .	59
<b>B</b>	<b>Monte Carlo Samples</b>	<b>61</b>
B.1	W+Jets . . . . .	61
B.2	Z+Jets . . . . .	62
B.3	$t\bar{t}$ . . . . .	62
B.4	QCD . . . . .	62
B.5	Diboson . . . . .	62
B.6	Drell Yan . . . . .	63
	<b>Bibliography</b>	<b>65</b>

# 1. Introduction

## 1.1 Standard Model of Particle Physics

The Standard Model (SM) of particle physics [1][2][3] is a renormalizable quantum field theory which today gives the best description of the known fundamental particles and their interactions: the electromagnetic, weak and strong nuclear force. Until now, gravitation which is at low energies negligible compared to the other forces, has not yet been incorporated into the theory.

### 1.1.1 Overview

Fermions are spin 1/2 particles (i.e. carrying spin =  $\frac{1}{2}\hbar$  where  $\hbar = \frac{h}{2\pi} = 6.582 \cdot 10^{-16} \text{ eV} \cdot \text{s}$  is the reduced Planck constant) and obey Fermi-Dirac statistics. They represent the elementary constituents of ordinary matter and are listed in table 1.1.

	1. Gen.	2. Gen.	3. Gen.	strong	em.	weak	grav.	Spin
<b>Leptons</b>	$\nu_e$	$\nu_\mu$	$\nu_\tau$	-	-	+	+	$\frac{1}{2}\hbar$
	$e^-$	$\mu^-$	$\tau^-$	-	+	+	+	$\frac{1}{2}\hbar$
<b>Quarks</b>	$u$	$c$	$t$	+	+	+	+	$\frac{1}{2}\hbar$
	$d$	$s$	$b$	+	+	+	+	$\frac{1}{2}\hbar$

Table 1.1: Quarks and Leptons

The 12 elementary fermions are divided into 3 generations: Each generation has a lepton  $l$  carrying an elementary charge  $1e = 1.602 \cdot 10^{-19} \text{ C}$  and a corresponding neutral leptonic neutrino  $\nu_l$ . Besides, there are also 3 families of quarks existing, each represented by two quarks: the up ( $u$ ) and down ( $d$ ) quark, the strange ( $s$ ) and charme ( $c$ ) quark and finally the top ( $t$ ) and bottom ( $b$ ) quark.  $u$ ,  $c$  and  $t$  (up-type quarks) carry an electric charge of  $+\frac{2}{3}e$ , whereas  $d$ ,  $s$  and  $b$  (down-type quarks) carry  $-\frac{1}{3}e$ .

Antiparticles, the antifermions, are assigned to each fermion and are not listed in table 1.1. They have the same quantum numbers as particles but opposite sign.

Interactions between the fermions are mediated via force carrier particles, the so-called gauge bosons. They carry spin 1 and thus obey Bose-Einstein statistics. In table 1.2 an overview of these bosons is given.

QFT	Gauge Symmetry	Interaction	Gauge Boson	relative strength	Spin
QCD	$SU(3)$	strong	8 Gluons $g$	1	$1\hbar$
QED	$U(1)$	electromagnetic	Photon $\gamma$	$1/137$	$1\hbar$
QFD	$SU(2)$	weak	$W^+, W^-, Z^0$	$10^{-14}$	$1\hbar$
-		gravitational	Graviton $G$ ?	$10^{-40}$	$2\hbar?$

Table 1.2: Fundamental interactions and their gauge bosons

From a mathematical point of view all interactions (except gravitation) are described by Quantum Field Theories (QFT): Quantum Chromodynamics (QCD), Quantum Electrodynamics (QED) and Quantum Flavourdynamics (QFD). They are all, more precisely, gauge theories and rely on certain symmetry groups. In all quantum field theories particles and fields are commonly described by a Lagrangian  $\mathcal{L}$ .  $\mathcal{L}$  is a function of both particles and fields and contains the internal symmetries. Gauge theories comply with local gauge symmetries: The solutions of the respective Lagrangian  $\mathcal{L}$  are invariant under certain *local* gauge transformations (i.e. phase transformations). This is known as local gauge invariance based on the gauge principle: By locally changing the phase of the wave function of a particle, one has to make sure the particle keeps satisfying the equations of its quantum state. Hence there is need to introduce external fields that eventually generate the gauge bosons. These gauge transformations correspond to symmetry operations and the invariance of the solutions characterizes a symmetry. The individual symmetry groups of the SM are Lie groups and altogether they form the symmetry group of the SM as the product of the Lie groups:

$$SU(3) \otimes SU(2) \otimes U(1)$$

As stated in the well known Noether Theorem, symmetries are strongly related to conservation laws. From the  $U(1)$  symmetry we can follow the conservation of electric charge.  $SU(2)$  infers the conservation of a weak charge and finally  $SU(3)$  states the conservation of colour charge.

### 1.1.2 Strong Interaction

The strong interaction is described by the QCD based on an unbroken  $SU(3)$  symmetry. The gauge bosons are 8 massless gluons, each of them coupling only to particles carrying a colour charge, i.e. they are acting upon quarks and themselves. Quark fields are forming triplets with a new internal quantum number: the colour charge which can be red, green or blue. Antiquarks carry anti-colours ( $\bar{r}, \bar{g}, \bar{b}$ ).

Due to confinement, coloured particles as quarks and gluons cannot exist as free particles, instead they occur in composite colourless hadrons. Hadrons can either be mesons which are made up of a quark and an antiquark pair or they can appear as baryons made of 3 quarks (e.g. proton made up of  $uud$ ).

At higher energies, quarks behave like free particles which is in contrast to the confinement and is known as "asymptotic freedom". In high-energy collisions in a particle collider, free quarks can for instance be created when two quarks become

separated. But still it is energetically more favourable when a new quark-antiquark pair appears from the vacuum and then combines with a temporary free quark by forming a hadron. So as a result one cannot see individual quarks in a detector, only jets coming from mesons and baryons are visible.

This formation process of hadrons out of quarks and gluons is called hadronization. It cannot be calculated perturbatively but there are some successful models of hadronization [4].

### 1.1.3 Electroweak Theory and Symmetry Breaking

The electromagnetic force is described by the QED based on a  $U(1)$  symmetry. It describes the interactions of electrically charged particles by exchange of photons, the massless gauge bosons of the electromagnetic interaction. The coupling strength is given by the elementary charge  $e$ .

Weak currents couple to massive, electrically charged gauge bosons  $W^\pm$ . The weak force has a unique property: Parity violation causes  $W^\pm$  only to couple to left-handed particles and right-handed antiparticles. Therefore, only these certain components of particles participate in weak interactions. Left-handed particles are grouped into  $SU(2)$  doublets ( $L$ ) whereas right-handed particles are represented by  $SU(2)$  singlets ( $R$ ):

$$L = \begin{pmatrix} \nu \\ e \end{pmatrix}_L, \quad R = (e)_R \quad (1.1)$$

One of the major successes of the Standard Model is the construction of the electroweak theory - a theory that combines the electromagnetic and the weak force. It is known as Glashow-Salam-Weinberg (GSW) Theory and is based on a local  $SU(2)_L \otimes U(1)_Y$  gauge symmetry. Here,  $SU(2)_L$  is the group of weak isospin transformations for lefthanded particles and  $U(1)_Y$  refers to phase transformations in weak hyper charge space. Due to the electric charge of the weak gauge bosons  $W^\pm$  the electromagnetic theory must be incorporated into this wider theory. The gauge bosons of the electroweak theory are 4 massless particles  $B_\mu, W_\mu^1, W_\mu^2, W_\mu^3$ . The two neutral bosons  $B_\mu$  and  $W_\mu^3$  mix and form a massless linear combination, the photon  $A^\mu$ , and an orthogonal massive linear combination, the neutral  $Z^\mu$  which corresponds to the  $Z^0$  boson:<sup>1</sup>

$$\begin{pmatrix} A^\mu \\ Z^\mu \end{pmatrix} = \begin{pmatrix} \cos \theta_w & \sin \theta_w \\ -\sin \theta_w & \cos \theta_w \end{pmatrix} = \begin{pmatrix} B_\mu \\ W_\mu^3 \end{pmatrix} \quad (1.2)$$

When the theory was developed, the  $Z^0$  boson was only predicted and at a later point it was finally discovered at CERN in 1983 [5].

However, the charged fields  $W_\mu^1$  and  $W_\mu^2$  also mix up and form the charged and massive  $W^-$  and  $W^+$  bosons.

Now the crucial problem we come across is the fact that we have 3 massive gauge bosons:  $Z^0$  and  $W^\pm$ . So far the  $SU(2)_L \otimes U(1)_Y$  symmetry does not allow the existence of massive gauge bosons because involving mass terms in the theory would destroy the symmetry - it is then no longer invariant under gauge transformations. This finally implies that the  $SU(2)_L \otimes U(1)_Y$  symmetry must be broken by a so-called

---

<sup>1</sup> $\theta_w$  denotes the weak mixing angle, the so-called Weinberg angle defined by the masses of  $W^\pm$  and  $Z^0$ :  $\cos \theta_w = \frac{m_W}{m_Z}$ .

Higgs mechanism. Gauge bosons acquire their masses by coupling to the Higgs field. The Higgs field is supposed to be a doublet of scalar, complex fields:

$$H(x) = \begin{pmatrix} H^+(x) \\ H^0(x) \end{pmatrix} \quad (1.3)$$

with a vacuum expectation value

$$H_{vac} = \frac{1}{\sqrt{2}} \begin{pmatrix} 0 \\ v \end{pmatrix} \neq 0. \quad (1.4)$$

The existence of a vacuum expectation value  $v \neq 0$  denotes the spontaneous symmetry breaking.

The Higgs mechanism can also provide an explanation for the fermion masses but the way the fermions acquire their masses through interaction with the Higgs field differs from the gauge bosons.

This mechanism leaves an elementary spin 0 particle behind: the Higgs boson. Until now the Higgs boson has not been discovered yet. Finding the Higgs boson is one of the major goals of particle physics up to date.

## 1.2 Open Issues Concerning the Standard Model

To sum up, the SM with its gauge structure

$$SU_C(3) \otimes SU_L(2) \otimes U_Y(1) \quad (1.5)$$

provides a good description of observations and experimental results. But still it bears some deficiencies one has to be aware of. This points to the question if the SM might be only part or an approximation of an even wider theory.

Problems and open issues of the SM include:

- 19 free parameters (neglecting the neutrino masses) that cannot be determined by theory
- Higgs Boson is not found yet
- Hierarchy problem: strong fine tuning of SM parameters is required to account for the fact that the weak scale is much lower than the Planck scale
- Is a unification of the 3 couplings  $\alpha_{em}$ ,  $G_F$  and  $\alpha_s$  possible?
- Why do we have exactly 3 generations of quarks and leptons, are there even more generations conceivable?
- What is the reason for the matter-antimatter asymmetry in our universe?
- What are Dark Energy and Dark Matter consisting of? Some astrophysical observations (e.g. discrepancies concerning rotational curves of galaxies) indicate a dark component of mass existing. The identity of this dark matter is still completely unknown, yet we can exclude all SM particles. The relic dark matter abundance could be explained by the existence of a stable particle of the order of the weak scale. This makes the Lightest Supersymmetric Particle (LSP) among various other particles a likely candidate.
- How to include gravitation into the theory in order to give a full description of all interactions existing? Is there a way to connect general relativity with quantum field theory, a so-called quantum gravitation?

## 1.3 Supersymmetry as a Possible Extension of the Standard Model

According to (1.5) interactions within the SM can be described by a rather complex structure.

This combination of various gauge fields is based on the existence of 3 independent symmetries and interactions and thus infers the existence of 3 independent coupling constants. Many attempts have been made to find some larger theory which is required to unify the three forces, the electromagnetic, the weak and strong interactions, at high energies. Those theories are summed up as the so-called Grand Unified Theories (GUTs). They all have in common that they are described by some wider symmetry group where the SM gauge interactions are already embedded and are merged into one single unified interaction. This of course implies the existence of a theory with a unified coupling constant.

It has been found out that for some (e.g. SU(5)) GUTs the coupling constants come very close but do not exactly meet at one point. However, this dilemma can be solved by the introduction of supersymmetry (SUSY).

### 1.3.1 SUSY - A Symmetry between Fermions and Bosons

Supersymmetry is a promising candidate to describe physics beyond the Standard Model.

It involves a symmetry which relates gauge bosons (B), the force carrier particles, to the fermions (F) matter consists of and treats them in a fully symmetric way.

Transformations between these two fundamental particle types are generated via

$$Q|F\rangle = |B\rangle, \quad Q|B\rangle = |F\rangle \quad (1.6)$$

where the generators Q induce a spin 1/2 transition. In other words, for each fermion there is a corresponding type of boson with the same internal quantum numbers but which differs by half a unit of spin and vice-versa. If SUSY is considered an unbroken theory, the SM particles and their superpartners have moreover the same mass.

In order to realize the supersymmetry between fermions and bosons, they both have to appear in the same Lagrangian along with supersymmetric transformations [6]:

$$\mathcal{L} = \underbrace{\partial_\mu \phi^* \partial_\mu \phi}_{(i)} + \underbrace{i\psi^\dagger \bar{\sigma}^\mu \partial_\mu \psi}_{(ii)} + \underbrace{F^+ F + \left( F \frac{\partial W}{\partial \phi} - \frac{1}{2} \psi^T \mathcal{C} \psi \frac{\partial^2 W}{\partial \phi^2} + c.c. \right)}_{(iii)} \quad (1.7)$$

where

- (i): kinetic energy of free boson ( $\phi$ )
- (ii): kinetic energy of free fermion ( $\psi$ )
- (iii): interaction terms

$\mathcal{C}$  is the conjugation operator and  $F$  denotes an auxiliary field which is defined by the equation of motion  $F^+ = -\frac{\partial W}{\partial \phi}$ .

Interactions between matter are determined by the Superpotential  $W(\phi)$ . In a Minimal Supersymmetric Standard Model (MSSM)  $W(\phi)$  is of the form [6]

$$W = \lambda_d[\dots] + \lambda_l[\dots] + \lambda_u[\dots] + \mu\bar{H}H \quad (1.8)$$

where the parantheses  $[\dots]$  stand for the fields of matter that correspond to the well known SM particles. The superpotential couplings  $\lambda_d, \lambda_l, \lambda_u$  correspond to the Yukawa couplings (couplings from fermions with the Higgs field) from the SM.

### 1.3.2 Field Content of the MSSM

Today a lot of models for supersymmetric theories exist. Among them the Minimal Supersymmetric Standard Model (MSSM) is considered as the minimal extension of the Standard Model. This means the number of new particles that appear within this theory framework is kept at the lowest level compared to the other models.

Within the MSSM, fermions have bosonic superpartners that are called sfermions and carry spin 0. While bosons have fermionic superpartners that carry spin 1/2 and are called bosinos. An overview of the SM particles along with their supersymmetric partners is given in table 1.3. In general, supersymmetric partners are denoted

Spin 0	Spin 1/2	Spin 1
$\tilde{l}, \tilde{\nu}$ (sleptons)	$l, \nu$	
$\tilde{q}$ (squarks)	$q$	
	$\tilde{g}$ (gluino)	$g$
	$\tilde{\gamma}$	$\gamma$
	$\tilde{Z}$	$Z$
$h, H, A$	$\tilde{h}, \tilde{H}$	
	$\tilde{W}^\pm$	$W^\pm$
$H^\pm$	$\tilde{H}^\pm$	

Table 1.3: Particles in MSSM

with  $\sim$ .

The neutral and charged Higgsinos  $\tilde{h}, \tilde{H}, \tilde{H}^\pm$  are the supersymmetric partners that correspond to the degrees of freedom of the Higgs field. Gauginos mix with the Higgsinos and form mass eigenstates called neutralinos and charginos:

- $\tilde{\gamma}, \tilde{Z}$  and the higgsinos  $\tilde{h}, \tilde{H}$  mix to 4 electrically neutral neutralinos  $\tilde{\chi}_1^0, \dots, \tilde{\chi}_4^0$
- $\tilde{W}^\pm, \tilde{H}^\pm$  mix to 2 electrically charged charginos  $\tilde{\chi}_{1,2}^\pm$ .

Regarding the fermions, each quark and each lepton is assigned to a squark and a slepton, respectively.

However, the situation for the Higgs field is more complicated: Whereas we require only one complex scalar Higgs doublet in the SM and therefore end up with only one Higgs boson, we now need to have two scalar Higgs doublets which finally result in



two Higgsinos. The reason for this are gauge anomalies a single Higgs boson would lead to. Each of the Higgs doublets  $H$  and  $\bar{H}$  couples to the superpotential in (1.8) and has its own vacuum expectation value.

The MSSM introduces a new symmetry, the R-Parity which leads to a new quantum number and can be defined as:

$$R_P = (-1)^{3B+L+2s} \quad (1.9)$$

where  $B$  = baryon number,  $L$  = lepton number and  $s$  = spin is. As SM particles only differ in the spin number from their superpartners, it follows that all SM particles have even parity  $R_P = +1$  whereas all superpartners have odd parity  $R_P = -1$ . R-parity violating processes may be possible but, however, if R-Parity is conserved, the lightest supersymmetric particle (LSP) is stable and assumed to be a neutralino. The LSP could be a candidate for Dark Matter, possibly accounting for the abundance of mass that is observed in the universe.

One of the biggest advantages of supersymmetry is its power to solve the fundamental Hierarchy problem which sets a serious theoretical concern: One would actually expect the mass of the Higgs boson to be around an energy scale where unification of electroweak and strong interaction can be achieved, i.e. at the GUT scale  $\lambda_{GUT} \sim 10^{16}$  GeV. It is necessary to apply excessive fine tuning in order to avoid a diverging Higgs mass due to radiative corrections. Supersymmetry solves this problem because bosonic terms are cancelled out by their fermionic superpartners. Thus this makes a fine tuning redundant since the Higgs mass is stabilized.

One of the challenges that even a minimal supersymmetric extension of the SM causes is the increase in free parameters we are faced with. Additionally to the already existing 19 parameters from the SM, we have to introduce 106 further parameters in order to end up with a full and consistent description of this new symmetry:

- 21 unknown masses of SUSY particles
- 41 mixing angles between chirality and mass states
- 43 CP violating phase angles
- 1 further vacuum expectation value arising from the second Higgs doublet.

All in all, this sums up to 125 free parameters that have to be determined. But as will be shown in the next section, several constraints can be put on this 125 dimensional parameter space.

### 1.3.3 Supersymmetry Breaking

Up to now, no supersymmetric particles have yet been observed. Therefore, SUSY must be a broken symmetry requiring the supersymmetric particles to be heavier than their SM partners:  $m_f < m_{\bar{f}}$ .

The mechanism of SUSY breaking is yet unknown - so far there are no fields existing within the MSSM that could lead (by evolving a vacuum expectation value  $\neq 0$ ) to a spontaneous symmetry breaking under conserved  $SU(3) \otimes SU(2) \otimes U(1)$  invariance. Hence all details concerning the breaking are banished into a so-called *hidden*

*sector* which is still a completely open issue. All we can say is that it contains fields which are able to cause a spontaneous SUSY breaking. This symmetry breaking is then mediated from the hidden sector to a *visible sector*, the latter constituting the unbroken SUSY, by certain Messenger fields. Several scenarios are qualified for this mediation. One of these possible scenarios are the gravity mediated SUSY breakings carrying the name SUGRA (**S**Uper **G**Ravity).

In all SUGRA models SUSY is broken by a Super Higgs Mechanism which leads to a very massive gravitino  $\tilde{G}$  with Spin 3/2. The mass of this gravitino determines the mass scale ( $\mathcal{O}(TeV)$ ) of other SUSY particles which is sensitive to the breaking scenario. In general, the neutralino is supposed to be the LSP.

As mentioned in (1.3.2), the MSSM, so far being a non-gravitational supersymmetric theory, involves the existence of a 125 dimensional parameter space. To reduce the number of free parameters, one can make the following simplifying assumptions where the Planck scale  $\Lambda_{Pl}$  of order  $\mathcal{O}(10^{19} \text{ GeV})$  is set equal to the GUT scale  $\Lambda_{GUT}$ .

A unification of all sfermion masses ( $m_0$ ) at the Planck scale as well as a unification of all gauge bosino masses  $m_{1/2}$  at the same scale can be assumed. Furthermore, assuming a universal Higgs-slepton-slepton and Higgs-squark-squark coupling  $A$ , this altogether sets an enormous constraint for SUGRA and implies the so-called minimal Super Gravity model (**m**SUGRA).

Taking into account 2 further parameters due to the existence of a second Higgs doublet in the MSSM, we end up with 5 breaking parameters which give a full description of masses and couplings of SUSY particles within the mSUGRA framework:

- $m_0$ : common sfermion mass
- $m_{1/2}$ : common gaugino mass
- $A$ : trilinear Higgs-sfermion-sfermion coupling
- $\mu_0$ : mixing parameter between both Higgs doublets in MSSM
- $\tan \beta = \frac{v_u}{v_d}$ : ratio of the vacuum expectation values from each Higgs doublet

So the main assumption of this model is a universality of all SUSY parameters at the Planck or the GUT scale, respectively.

SUSY searches within mSUGRA models are therefore performed by scanning the 5 dimensional parameter space ( $m_0, m_{1/2}, \tan \beta, A, \mu_0$ ) by choosing different sets of parameters and comparing the expected to the observed limits (i.e. cross sections). This makes it possible to exclude certain points within the parameter space, for instance certain mass combinations of  $m_0$  and  $m_{1/2}$ .

The search for supersymmetry was already performed at different experiments, among these were the ones at LEP and Tevatron yielding no success so far, though. The Large Hadron Collider (LHC) at CERN started running in November 2009 with a design centre-of-mass energy of 7 TeV. It is expected that, if SUSY at the weak scale exists, some superpartners must not be too heavy and can be produced at the LHC [7].

## 2. LHC and the ATLAS Experiment at CERN

The Large Hadron Collider (LHC) [8] is a particle accelerator which was built to reach the world's highest collision energies up to now by colliding either protons ( $p - p$  collisions) or two opposite beams of lead nuclei ( $Pb - Pb$  collisions). It aims at finding solutions for some yet unsolved problems within the field of particle physics and has a high potential to shed light on new physics phenomena ranging from Dark Matter, the search for the still undetected Higgs boson and finally to proving the existence of Supersymmetry.

The LHC is located at CERN (European Organization for Nuclear Research) which is the world's largest physics laboratory dealing with fundamental research. It is situated close to Geneva, more exactly at the border between Switzerland and France. The LHC finally successfully started running in November 2009 with a centre-of-mass energy of 900 GeV. The first planned  $p - p$  collisions at half design energy, 7 TeV, took place on March 30, 2010 which set a new record — an energy that has never been reached before in particle collisions up to this date.

On June 17, 2011 the LHC reached an integrated luminosity of  $1 \text{ fb}^{-1}$  of  $p - p$  collisions. This is a huge amount of data to be analysed and testifies an outstanding performance until now.

After 2 successful years of running at half the design energy, the LHC will be closed down from the end of 2012 until 2014 in order to prepare it for running at full design energy, namely a centre-of-mass energy of 14 TeV.

### 2.1 The LHC

The LHC [9] has a circumference of 27 km long and is located at 100 m underground. It uses the same tunnel (diameter 3.0 m) as the former accelerator LEP (Large Electron Positron Collider) that was shut down at the end of 2000 and used to be the most powerful electron collider.

Inside the LHC, two beams of protons, rotating into opposite directions, will be accelerated to a design energy of 7 TeV per beam. Bunches containing up to a billion

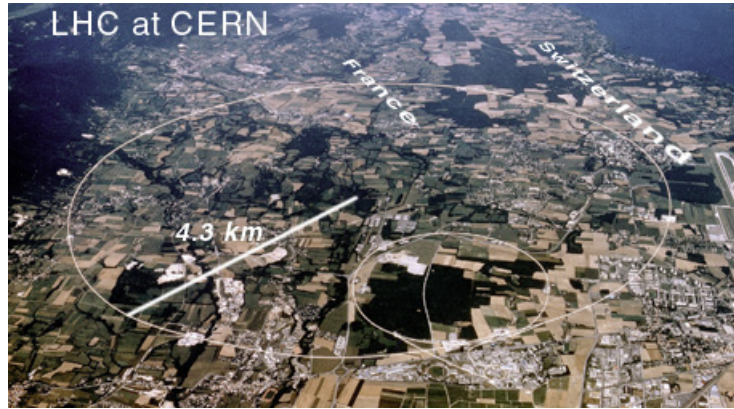


Figure 2.1: LHC at CERN

protons will collide about 40 million times per second and result in proton-proton collisions of 14 TeV. The design luminosity of the collider is  $10^{34} \text{ cm}^{-2}\text{s}^{-1}$ . Achieving high luminosity bears a higher potential for discovering new physics phenomena. This is due to the fact that some of the processes that are to be observed can be extremely rare so enough ordinary collisions are needed to provide reasonable statistics. Since the following relation holds

$$N = \sigma \int L dt \quad (2.1)$$

where  $\int L dt$  is called *integrated* luminosity, the *instantaneous* luminosity  $L$  is proportional to the event rate ( $\frac{dN}{dt}$ ). Obtaining high luminosities, like the design luminosity of the LHC, poses a demanding technical challenge, though.

Before getting into the main LHC ring, the energy of the protons is increased successively in several preaccelerators [10]. The proton beam is boosted in each accelerator up to a certain energy and afterwards injected into the following accelerator. In figure 2.2 an overview of the complex accelerator system at CERN is given.

Hydrogen atoms serve as a source for protons by simply removing the electron from the atom. Then the protons are passing a series of systems before finally passing the LHC ring.

First low energy particles are generated by a linear accelerator LINAC3 (LINAC2 in the case of ions that are needed for one of the experiments). Afterwards the protons are forwarded into the Proton Synchrotron (PS) booster (Leir for ions, respectively) and again from this system transferred next to the Proton synchrotron (PS). Here, they are accelerated up to an energy of 25 GeV, succeeded by the next accelerator, the Super Proton Synchrotron (SPS). At this point the particles reach an energy up to 450 GeV before they are finally injected into the main LHC ring. Now they will circulate 20 minutes until they reach their design energy of 7 TeV each.

In order to account for the fact that two oppositely directed magnetic fields are required to make the beams counter-rotating, both proton beams are guided through separate beam pipes at ultrahigh vacuum. This is necessary to avoid collisions with

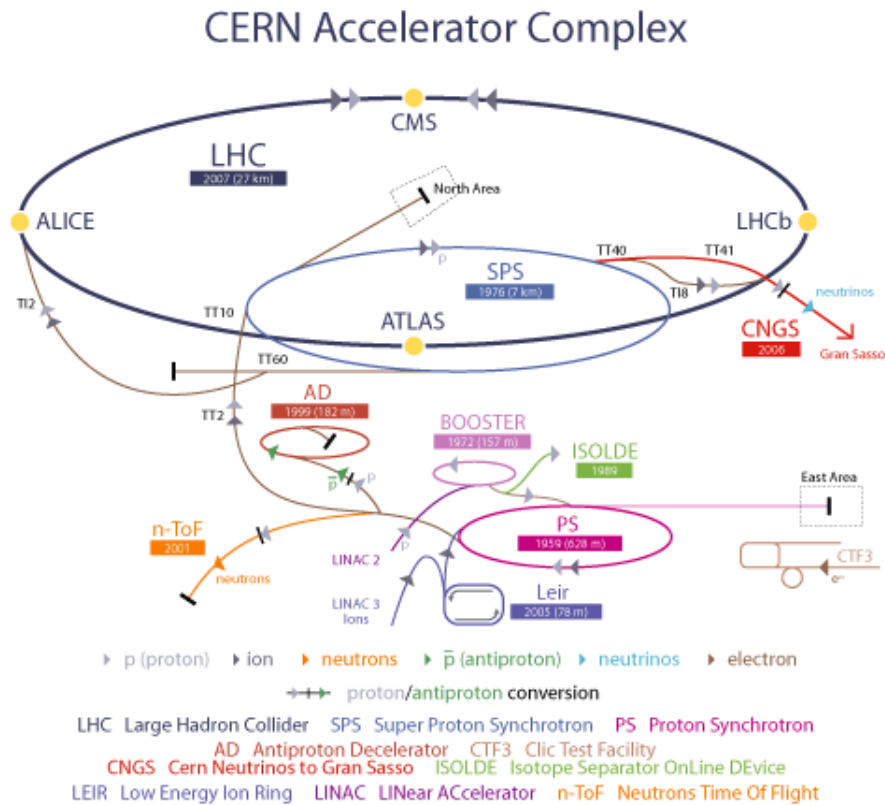


Figure 2.2: CERN accelerator complex [10]

gas molecules. The protons are kept on their track by superconductive electromagnets resulting in a strong magnetic field. To achieve this superconductive state the magnets must be cooled down to an energy of  $-271^{\circ}\text{C}$ . Therefore, many tons of liquid helium are needed to keep the magnets at their operating temperature. When travelling through the ring, 1232 dipole magnets keep the protons in their orbits whereas 392 quadrupol magnets are used to focus the beam. This is required to get sufficiently dense proton bunches since a high rate of collisions needs small bunch size at the various interaction points. These points around the accelerator ring where the collisions take place correspond to the position of the particle detectors. Of course, at these collision points there are no magnetic fields present so the beams are moving straight and can be brought together in order to collide [8].

The LHC is hosting 4 main experiments and furthermore 2 smaller ones. Among the main experiments there are two general purpose detectors:

- ATLAS (**A** Toroidal **LHC** Apparatu**S**)
- CMS (**C**ompact **M**uon **S**olenoid)

These two large experiments were built to investigate a wide range of physics, looking for signs of new physics, e.g. the existence of supersymmetry or eventually the discovery of the SM Higgs boson.

Another two detectors are medium-sized experiments that aim to examine specific phenomena:

- ALICE (**A** **L**arge **I**on **C**ollider **E**xperiment): studying quark-gluon plasma. This state of matter is assumed to have existed soon after the Big Bang. For this purpose, the LHC is colliding lead ions.
- LHCb (**L**arge **H**adron **C**ollider **b**eauty): investigating the CP violation by studying the b quark ('beauty' stands for 'bottom').

Finally there are still two small-sized experiments having a very specific goal setting:

- TOTEM (**T**OTAL **E**lastic and diffractive cross section **M**easurement): measuring  $p - p$  interaction cross section, detailed study of proton structure
- LHCf (**L**arge **H**adron **C**ollider **f**orward): studying cosmic ray physics.<sup>1</sup>

## 2.2 The ATLAS Detector

The ATLAS project [12][8][13]) is an international collaboration with 38 countries participating.

As mentioned, the ATLAS detector is one of the two general purpose detectors that will study  $p - p$  interactions on a wide range of physics, looking especially for discovery of physics beyond the Standard Model.

High  $p - p$  interaction rates, particle multiplicities and high energies are setting an enormous technical challenge in constructing a sophisticated particle detector like ATLAS. After a collision took place the decay products of the short-lived particles can be detected and allow to infer the processes they originate from.

Multi-component detectors like ATLAS are constructed to meet these high demanding challenges. They make it possible to investigate the decay products within different layers of the detector. Each layer has a certain task which is mainly to measure momenta or energies of particles and to identify particle types, respectively.

Figure 2.3 shows a schematic diagram of the ATLAS detector.

The ATLAS detector can be described by 4 large components which are later on explained in more detail: The Inner Detector measures momenta of charged particles. It is followed by the calorimeter (electromagnetic/hadronic) that is responsible for measuring the energies of particles. The muon detectors identify muons. The magnet system (Solenoid and Toroid) is required to bend charged particles in order to infer their momenta.

Regarding its dimensions, the detector has a total length of 44 m, a diameter of 22 m and weighs around 7000 tons. It has a cylindrical shape which is due to the fact that after a collision the particles radiate into all directions.

---

<sup>1</sup>The small LHCf collaboration studies  $p - p$  collisions that are under laboratory conditions similar to the collisions of ultra-high-energy cosmic rays with the earth's atmosphere. Ultra-high-energy cosmic rays ( $> 10^{18}$  GeV) are very rare and not fully understood yet. LHCf makes measurements which are used by larger cosmic ray experiments to investigate how and where these ultra-high-energy cosmic rays are produced [11].

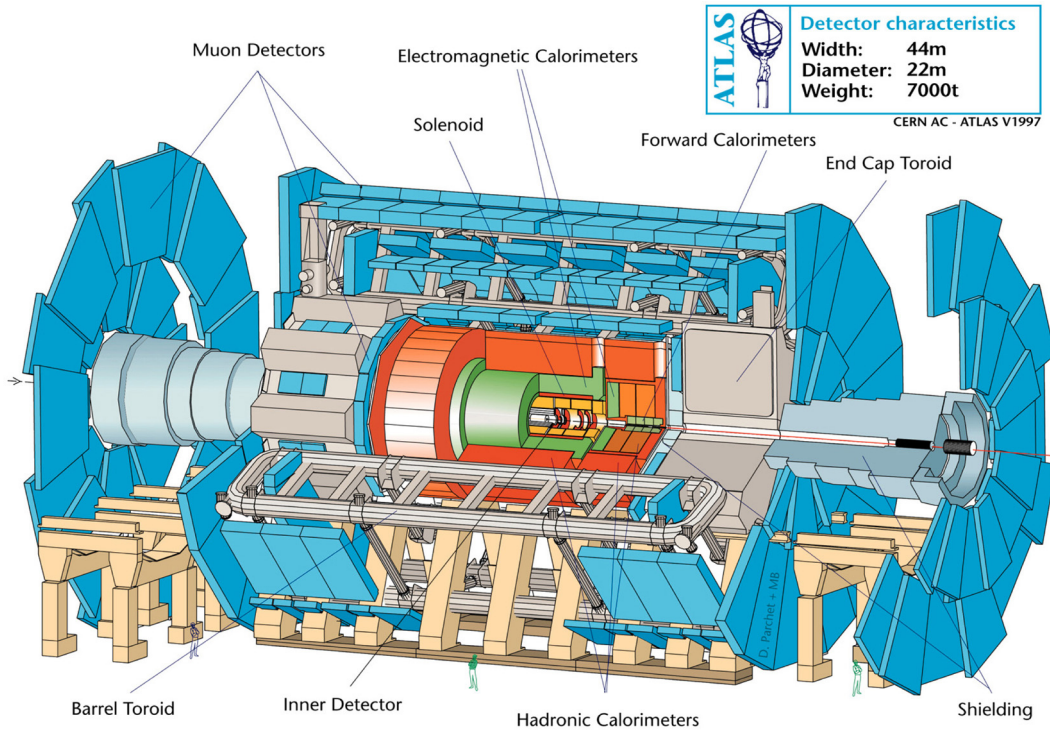


Figure 2.3: ATLAS detector

### 2.2.1 Coordinate System

The cylindrical shape of the ATLAS detector suggests the use of cylindrical coordinates. The collision point is defined as the origin of the coordinate system. The x-axis and y-axis lie on a plane transverse to the beam direction. While the x-axis is pointing from the collision point to the centre of the LHC ring, the y-axis is pointing upwards. The z-axis points towards the beam direction and the positive z direction is determined by considering a right-handed coordinate system. Now two spherical coordinates are introduced: The azimuthal angle  $\phi$  is commonly measured around the beam axis where  $\phi = 0$  corresponds to points lying on the positive x-axis and  $\phi$  increases clock-wise into positive z direction. The spherical angle  $\theta$  on the other hand points from the beam axis i.e. it is measured around the x-axis.  $\theta = 0$  corresponds to the points lying on the positive z-axis. A new variable, the pseudorapidity  $\eta$ , is defined as

$$\eta = -\log\left(\tan\frac{\theta}{2}\right) \quad (2.2)$$

Transverse momentum  $p_T$ , transverse energy  $E_T$  as well as missing transverse energy  $E_T^{miss}$  are defined as perpendicular to the beam axis of the LHC. Considering a pseudorapidity-azimuthal angle space the distance is defined as

$$\Delta R = \sqrt{\Delta\eta^2 + \Delta\phi^2}. \quad (2.3)$$

### 2.2.2 Components of the ATLAS Detector

The various detector components are layered around the beam pipe which is running along the centre of the detector (with the collision point being in the middle).

### 2.2.2.1 Inner Detector

The main function of the Inner Detector (figure 2.4) is measuring the directions, momenta and signs of the charged particles. The detector is filled with highly segmented sensing devices. This is required to determine the trajectories of each charged particle very accurately and reasons the name Inner *Tracker*. The momentum and vertex resolution requirements are extraordinary demanding as approximately 1000 particles are emerging from the collision point every 25 ns within  $|\eta| < 2.5$ . This implies a huge track density and only high-precision measurements with fine detector granularity can deal with.

The Inner Detector has several sublayers. It consist of three types of sensors: The Pixel detectors, SemiConductor Trackers (SCT) as well as a Transition Radiation Tracker (TRT). All these sensors are embedded in a magnetic field parallel to the beam axis.

The innermost part of the Inner Detector is built of Pixel detectors. They consist of thin wafers of silicon, being subdivided into tiny regions ('pixels') and measuring  $(50 \times 400) \mu\text{m}$  each. Each time a charged particle traverses a silicon wafer a signal is produced that allows to identify which pixel exactly has been traversed. This sets a highly accurate measure of the position of a particle.

The next part surrounding the Pixel detectors are the SCT trackers. These are 8 layers of Silicon microstrip detectors that serve to provide additional position measurements not immediately close by the collision point. These 8 layers are again subdivided into long and narrow strips, each strip being about  $80 \mu\text{m}$  wide and several centimetres long. When particles traverse the strip detector a signal identifies which strip has been traversed and this provides a 3-dimensional position measurement. The SCT covers  $|\eta| < 2.5$ .

The outermost component of the Inner Detector is the so-called Transition Radiation Tracker and consists of straw-tube tracking detectors (4 mm diameter). The tubes in the barrel part run parallel to the beam pipe whereas the tubes positioned in the end-caps are oriented radially. The TRT provides 2-dimensional measurement points having a resolution of 0.170 mm for tracks of charged particles with  $|\eta| < 2.0$ .

### 2.2.2.2 Calorimeter

The calorimeter provides a measurement of the total energy of the particles by absorbing them. Depending on the particle type their energy is either measured in the electromagnetic calorimeter or in the hadronic calorimeter.

**Electromagnetic (EM) Calorimeter.** Here, the energies of electromagnetically interacting particles ( $e^\pm, \gamma$ ) are measured. These particles are producing electromagnetic showers through interaction with matter: Whenever an electron (or positron) is deflected by the electric field of atomic nuclei, it emits bremsstrahlung. This photon again produces via pair production  $e^+e^-$  pairs which in turn can radiate photons. This cascade process allows to infer the energy of the initiating particle because it is proportional to the number of final  $e^+e^-$  pairs.

The EM calorimeter consists of a barrel part that covers the region  $|\eta| < 1.475$  and two end-cap components covering  $1.375 < |\eta| < 3.2$ . They are both housed in their own cryostat. The EM calorimeter is a lead-LAr (liquid Argon) detector with lead plates (1.5 mm thick) that serve as energy absorbing material and liquid Argon gaps



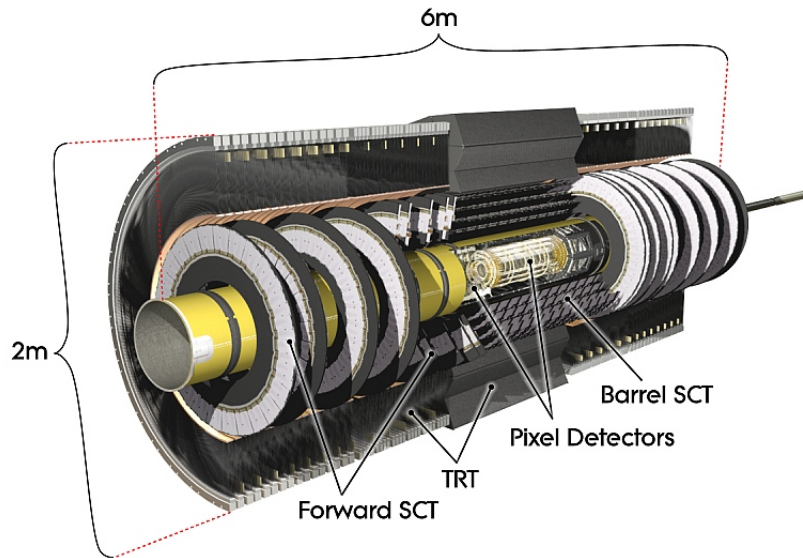


Figure 2.4: Inner detector [14]

(4 mm thick) that are subjected to an electric field.

**Hadronic Calorimeter.** The hadronic calorimeter is absorbing energies from particles that are passing the EM calorimeter and interact via the strong force, i.e. hadrons (e.g. protons, neutrons, pions, kaons, etc.). Again the hadrons are interacting with dense material and therefore produce hadronic showers of charged particles whose deposited energy can finally be measured.

The hadronic calorimeter surrounds the EM calorimeter and consists of 3 subsystems. The tile calorimeter is placed immediately outside the envelope of the EM calorimeter. It consists of steel plates that serve as absorbing material and scintillating tiles (3 mm thick) that serve as active material. The scintillator produces signals proportional to the number of hadronic shower particles. The subdivision into tiles takes a correlation between the amount and the location of the energy deposit into account.

The LAr hadronic end-cap calorimeter is directly located behind the LAr EM end-cap calorimeter and shares the same LAr cryostat. The main difference between both is that lead plates are now replaced by copper plates due to the hadronic showering process.

To complete the LAr calorimeter, the Liquid Argon Forward calorimeter is integrated into the end-cap cryostats close to the beampipe and is made from copper and tungsten.

### 2.2.2.3 Muon Detector

The Muon detector as the outer layer can only be reached by muons and neutrinos. Neutrinos pass the calorimeter system since they are neither electromagnetically nor strongly interacting. Muons on the other hand are electromagnetically interacting but since they are much heavier than electrons they have less bremsstrahlung and

therefore do not produce this kind of electromagnetic shower. Muons can be detected while the weakly interacting neutrinos escape the detector. Their existence can be inferred from missing energy.

The muon system is a very large tracking system, extending from 4.25 m (radius of the calorimeter) out to the radius of the full detector (11 m).

The low barrel region ( $|\eta| < 1.0$ ) is covered by a large barrel toroid system. In this region muons are measured in three cylindrical layers of chambers going around the beam axis. In the transition region as well as in the end-caps the chambers are again installed in three layers but now perpendicular to the beam axis. Precision measurements of muon tracks are provided by Monitored Drift Tubes (MDTs) over most of the  $\eta$ -range. These drift tubes (3 cm diameter) are filled with a gas mixture Ar:CO<sub>2</sub> = 93:7. At large pseudorapidities ( $2 < |\eta| < 2.7$ ) MDTs are replaced by Cathode Strip Chambers (CSCs) having higher granularity. They are multiwire proportional chambers [15] and filled with a gas mixture Ar:CO<sub>2</sub> = 80:20.

A region of  $|\eta| < 2.4$  is covered by the trigger system. Here Resistive Plate Chambers (RPCs), i.e. gaseous parallel electrode-plates, are used in the barrel region while Thin Gap Chambers (TGCs), i.e. multi-wire proportional chambers, are used for triggering in the end-cap regions.

#### 2.2.2.4 Magnet System

The purpose of magnets present in the detector is the bending of charged particles. ATLAS has a system of four large superconducting magnets.

**Central Solenoid.** The central solenoid is surrounding the Inner Detector. It has a length of 5.3 m and is designed to provide a 2 T magnetic field for the Inner Detector to allow even high energetic particles to be sufficiently bent.

**Barrel Toroid.** The system of 3 large toroids generates the magnetic field for the muon spectrometer. One barrel toroid produces a toroidal magnetic field of 0.5 T in the central region while two end-cap toroids produce a magnetic field of 1 T in the endcap regions.

To summarize the effect of the detector layers, the particle identification and interaction is illustrated in figure 2.5.

#### 2.2.2.5 Trigger Architecture

Due to limited data storage and processing capabilities it is not possible to record all collision data for analysis. The ATLAS trigger system [15] is based on three levels: The L1 trigger, L2 trigger and event filter. The final rate of recorded collision data is reduced to 200 Hz.

The L1 trigger is hardware based and selects leptons (including  $\tau$ 's), photons and jets with high transverse momenta. The selection is only based on a limited amount of the total detector information: Muons are identified using trigger chambers in the muon spectrometer (L1muon), whereas leptons and jets are selected using calorimeter triggers (L1calo). Results from L1muon and L1calo are fed to the central part of the L1 trigger system, the Central Trigger Processor (CTP). The calculation of trigger decision is made in  $< 2.5 \mu\text{s}$  and reduces the rate to 75 kHz. The L1 trigger also defines Regions-of-Interest (RoIs's) in  $(\eta, \phi)$  and passes them to the next high-level

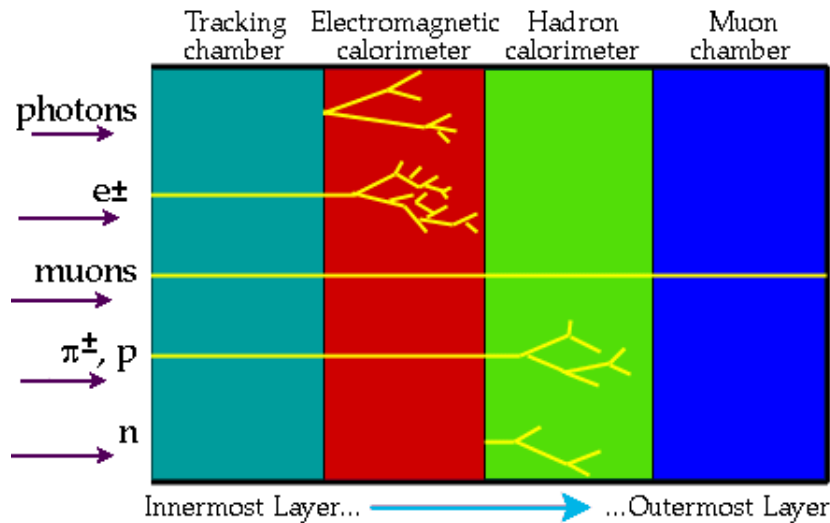


Figure 2.5: Particles passing layer elements [13]

trigger, the L2 trigger. L2 is a software based trigger that uses all available data within the RoI's, i.e. it can also access information from the Inner Tracker. The trigger rate is reduced to 3.5 kHz while an event is processed in  $\sim 40$  ms by the L2 menus. The final selection is done by the event filter which uses offline analysis procedure. It has a processing time of 4 s and reduces the final event rate to 200 Hz.

### 2.2.3 The LHC Computing Grid

Although the event rate was highly reduced by the trigger system, still huge amounts of collision data have to be stored and accessed for physics analysis use. This is accomplished through the LHC Computing Grid (LCG) [7]. It is based on an infrastructure where computer power and data storage capacity are commonly provided by various computing centres around the world. These off-site computing centres are cooperating with CERN on-site computing facilities.

The LCG project relies on several “Tiers”: Tier-0 is a computing facility hosted at CERN where raw data output from the high-level trigger is processed and reconstructed. A copy of these data is stored at large powered computer centres around the world, called Tier-1. The data can be passed on to several sites (Tier-2) mainly used for analysis and each linked to the respective Tier-1 centre. The final level also used for analysis, the Tier-3 centre, constitutes individual group clusters in research institutes.

The work in this thesis was carried out to a great extent using the grid. The analysis is based on the ROOT framework and uses D3PDs as input files <sup>2</sup>.

<sup>2</sup>D3PDs are n-tuples using only a limited amount of information stored in the AODs (Analysis Object Data). AODs are output from the reconstructed raw data [16].



# 3. SUSY Searches at ATLAS in the Dilepton Channel

## 3.1 Introduction

In R-parity conserving SUSY models sparticles can only be produced in pairs otherwise the symmetry would be violated. After two superpartners have been created in a  $p - p$  collision, each of them quickly decays into other short-lived supersymmetric particles as well as into ordinary particles like quarks (i.e. hadronic jets) and leptons. The supersymmetric decay chain always ends up with the Lightest Supersymmetric Particle (LSP) in the final state. Unlike all other superpartners the LSP is stable, and in the mSUGRA model considered in this thesis, is the neutralino ( $\chi_i^0$ ) [17]. Since the LSP is not interacting it cannot be detected and causes a significant amount of transverse missing energy ( $E_T^{miss}$ ) in the event.

To sum up, a typical SUSY signature are events that have a presence of

$$n \text{ jets} + m \text{ leptons} + E_T^{miss}$$

in the final state, where  $n, m = 0, 1, \dots$

An overview on some of the decay modes with their respective signature is given in table 3.1.

## 3.2 The Dilepton Channel

The work presented in this thesis is based on an analysis focussing on the dilepton channel. This channel is a very promising discovery channel for SUSY at the LHC. Many supersymmetric decays end up with two leptons in the final state. An important source of isolated leptons are the decay of charginos  $\tilde{\chi}_i^\pm$  or neutralinos  $\tilde{\chi}_i^0$ .

Creation	The main decay modes	Signature
• $\tilde{g}\tilde{g}, \tilde{q}\tilde{q}, \tilde{g}\tilde{q}$	$\left. \begin{array}{l} \tilde{g} \rightarrow q\bar{q}\tilde{\chi}_1^0 \\ q\bar{q}'\tilde{\chi}_1^\pm \\ g\tilde{\chi}_1^0 \\ \tilde{q} \rightarrow q\tilde{\chi}_i^0 \\ \tilde{q} \rightarrow q'\tilde{\chi}_i^\pm \end{array} \right\} \begin{array}{l} m_{\tilde{g}} > m_{\tilde{q}} \\ m_{\tilde{g}} > m_{\tilde{q}} \end{array}$	$\cancel{E}_T + \text{multijets (+leptons)}$
• $\tilde{\chi}_1^\pm \tilde{\chi}_2^0$	$\begin{array}{l} \tilde{\chi}_1^\pm \rightarrow \tilde{\chi}_1^0 \ell^\pm \nu, \tilde{\chi}_2^0 \rightarrow \tilde{\chi}_1^0 \ell \ell \\ \tilde{\chi}_1^\pm \rightarrow \tilde{\chi}_1^0 q\bar{q}', \tilde{\chi}_2^0 \rightarrow \tilde{\chi}_1^0 \ell \ell, \end{array}$	trilepton + $\cancel{E}_T$ dileptons + jet + $\cancel{E}_T$
• $\tilde{\chi}_1^+ \tilde{\chi}_1^-$	$\tilde{\chi}_1^+ \rightarrow \ell \tilde{\chi}_1^0 \ell^\pm \nu$	dilepton + $\cancel{E}_T$
• $\tilde{\chi}_i^0 \tilde{\chi}_i^0$	$\tilde{\chi}_i^0 \rightarrow \tilde{\chi}_1^0 X, \tilde{\chi}_i^0 \rightarrow \tilde{\chi}_1^0 X'$	dilepton+jet + $\cancel{E}_T$
• $\tilde{t}_1 \tilde{t}_1$	$\begin{array}{l} \tilde{t}_1 \rightarrow c\tilde{\chi}_1^0 \\ \tilde{t}_1 \rightarrow b\tilde{\chi}_1^\pm, \tilde{\chi}_1^\pm \rightarrow \tilde{\chi}_1^0 q\bar{q}' \\ \tilde{t}_1 \rightarrow b\tilde{\chi}_1^\pm, \tilde{\chi}_1^\pm \rightarrow \tilde{\chi}_1^0 \ell^\pm \nu, \end{array}$	2 noncollinear jets + $\cancel{E}_T$ single lepton + $\cancel{E}_T + b's$ dilepton + $\cancel{E}_T + b's$
• $\tilde{l}_i, \tilde{l}_j, \tilde{\nu}\tilde{\nu}$	$\begin{array}{l} \tilde{\ell}^\pm \rightarrow \ell^\pm \tilde{\chi}_i^0, \tilde{\ell}^\pm \rightarrow \nu_\ell \tilde{\chi}_i^\pm \\ \tilde{\nu} \rightarrow \nu \tilde{\chi}_1^0 \end{array}$	dilepton + $\cancel{E}_T$ single lepton + $\cancel{E}_T$

Table 3.1: Supersymmetric decay modes and their signature [17]

The main decay processes that can lead to a signature with two leptons are listed in the following [18]:

- (1.)  $\tilde{\chi}_i^0 \rightarrow l^\pm \nu \tilde{\chi}_j^\mp$
- (2.)  $\tilde{\chi}_i^\pm \rightarrow l^\pm \nu \tilde{\chi}_j^0$
- (3.)  $\tilde{\chi}_i^0 \rightarrow l^\pm l^\mp \tilde{\chi}_j^0$
- (4.)  $\tilde{\chi}_i^\pm \rightarrow l^\pm l^\mp \tilde{\chi}_j^\pm$

A two lepton event can either be obtained with the leptonic decays of neutralinos (3.) or charginos (4.) or by the two independent decays (1.) and (2.) giving one lepton each. In figure 3.1 three different gluon gluon collisions with sparticle production and their supersymmetric cascade decays are shown. They all have a signature of two leptons, several jets and  $E_T^{miss}$  in the final state. The two cascade decays on the bottom are an example for the leptonic neutralino decay presented in chain (3.). The cascade decay on the top shows an example of chain (2.).

Two final state leptons can either be same-sign (SS) or opposite-sign (OS) and they can have equal or different flavour: One distinguishes the channels  $ee, \mu\mu$  and  $e\mu$ , i.e. two electrons, two muons or one electron and one muon, respectively. This makes 6 possible configurations when investigating the dilepton channel in detail. Same-sign lepton pairs can only be produced by the single lepton decay processes (1.) and (2.) that have to occur both in the same event. There are more possibilities for opposite-sign lepton pairs to be produced in SUSY decays since all decay chains can contribute in this case. Therefore the signal in the OS channel is higher but there are also more background processes from SM.

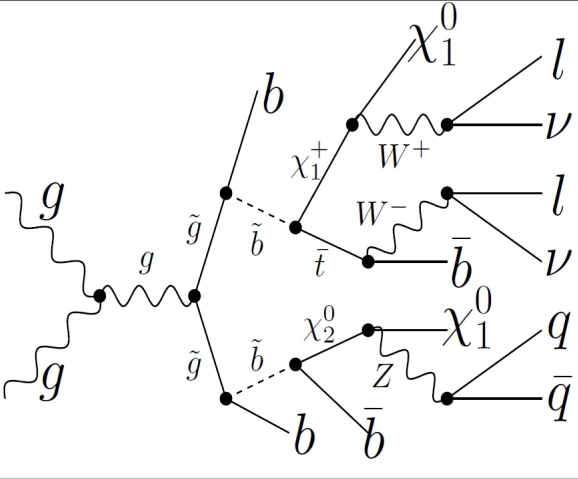
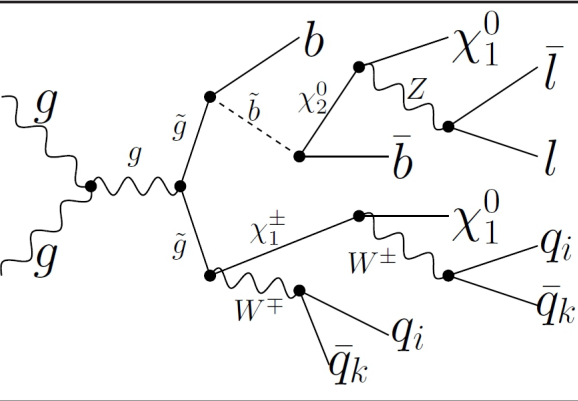
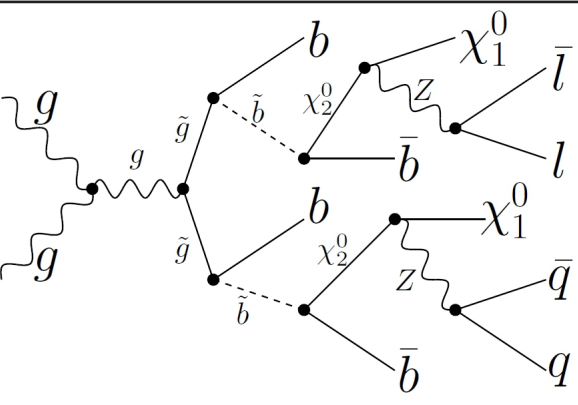
Process	final states
	$2\ell$ $2\nu$ $6j$ $\cancel{E}_T$
	$2\ell$ $6j$ $\cancel{E}_T$
	$2\ell$ $6j$ $\cancel{E}_T$

Figure 3.1: Supersymmetric cascade decays with presence of 2 leptons in final state [17]

### 3.3 Important Backgrounds to Dilepton Searches

The main backgrounds to a dilepton search are [18]:

$t\bar{t}$ .  $t\bar{t}$  is the dominant background at high  $E_T^{miss}$  for the dilepton channel. The semileptonic  $t\bar{t}$  decay is dominant in the SS channel whereas the fully leptonic one is dominant in the OS channel. As can be seen in figure 3.2, in semileptonic  $t\bar{t}$  decays one lepton comes from the W decay while the second lepton originates from the b jet. The hadronic decay of the W boson produces jets while the neutrinos from the leptonic W decay produce the missing energy signature. In case of the fully leptonic  $t\bar{t}$  decay both W bosons are decaying leptonically.

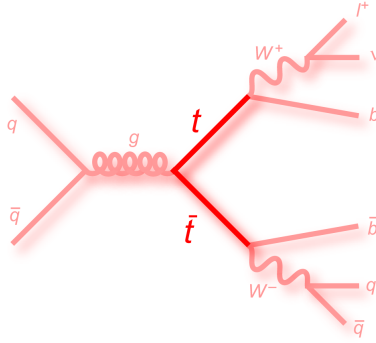


Figure 3.2: Semileptonic  $t\bar{t}$  decay

**Z+Jets.** In case of Z+jets, both leptons come from the Z decay into OS lepton pairs:  $Z \rightarrow l^+l^-$ . In case of the SS channel, the charge of the second lepton is misidentified.

**W+Jets.** One lepton comes from the W decay into a lepton and a neutrino:  $W \rightarrow l\nu$ , the second lepton is a misidentified light jet.

**Wbb+Jets.** One lepton originates from the  $W \rightarrow l\nu$  decay while the other lepton comes from the b-quark decay.

**Dibosons.** Diboson events WZ and ZZ produce at least three leptons. If one of the leptons was not reconstructed it is possible to obtain two leptons (OS/SS) in the final state. Regarding WW pair production we can obtain two SS leptons from  $W^\pm W^\pm$  or from  $W^\pm W^\mp$  due to charge misidentification. In case of OS the two leptons are from  $W^\pm W^\mp$ .

**QCD.** Dilepton events can be found in multijet events when 2 jets are misidentified as leptons (referred to as *fake* leptons). The QCD background has a very high cross section but the probability to have 2 fake leptons in one event is rather small. It is hard to model this background component with Monte Carlo (MC). The QCD component is often estimated using data.

In this thesis an analysis will be presented to estimate the fake electron background in the signal region directly using data. The method is described in detail in the next chapter.



## 3.4 Object Reconstruction and Identification

Physics analysis at the LHC requires excellent particle reconstruction and identification. To provide a basis for the following chapters the reconstruction of electrons, jets and muons <sup>1</sup> shall be explained in detail.

### 3.4.1 Electrons

#### 3.4.1.1 Reconstruction

For the reconstruction of electrons [19][20], the information from both the calorimeter and the Inner Tracker is used. At present, three electron reconstruction algorithms are implemented in the ATLAS offline software: The Standard electron algorithm is applied to reconstruct high  $p_T$  isolated electrons. The second one, responsible for soft electron reconstruction, is dedicated to low  $p_T$  electrons. A further algorithm is available for electrons lying in the forward region of the ATLAS detector.

**Standard Electron Algorithm.** This algorithm (`egammaBuilder`) reconstructs high  $p_T$  isolated electrons and is a cluster based algorithm. It first creates seed clusters (electromagnetic clusters reconstructed in the calorimeter) that are required to have an energy greater than 2.5 GeV and are associated to the tracks of charged particles reconstructed in the Inner Detector. A reconstructed object is identified as an electron if at least one reconstructed track matches a seed cluster after extrapolation to the EM calorimeter. The track-to-cluster matching performed by the algorithm is limited to the region of the tracker detector ( $|\eta| < 2.5$ ).

**Soft Electron Algorithm.** The algorithm `softeBuilder` is a track based algorithm that reconstructs non-isolated electrons having low energies of only a few GeV. Hereby tracks in the Inner Detector are used as a starting point and are extrapolated to the EM calorimeter where a cluster is formed around the extrapolation point. Again, reconstruction of the electron is performed by a track-to-cluster matching.

**Forward Electron Algorithm.** The algorithm `egammaForwardBuilder` reconstructs and identifies electrons that lie within  $2.5 < |\eta| < 4.9$ , the forward region of the detector. This algorithm can only use information from the calorimeter since the Inner Tracker region is limited to  $|\eta| < 2.5$ . It is based on topological clusters and provides energy and position measurement. An electron is reconstructed in the forward region of the EM calorimeter if a cluster with  $E_T < 5$  GeV exists.

#### 3.4.1.2 Identification

There are three reference sets of cuts that define identification criteria for electrons at ATLAS [21][22][19] and will play a major role in this work. They are referred to as *loose*, *medium* and *tight* identification criteria and have increasing power in rejecting background.

**Loose Electrons.** Loose electrons are based on a loose set of cuts which provides among the three sets the best identification efficiency but also the lowest background rejection. The electron identification is based on limited information from the EM

---

<sup>1</sup>taus are not subject of this work

calorimeter. Only shower-shape variables which were derived from the middle layer of the calorimeter and cuts on the hadronic leakage are applied for the loose selection.

**Medium Electrons.** The medium set of cuts is tightened compared to the loose cuts by using more calorimeter information (cuts on strips in the first layer are now included) and by introducing track quality requirement cuts. This results in a better jet rejection but reduces the identification efficiency with respect to loose electrons by  $\sim 10\%$ .

**Tight Electrons.** Tight electrons are based on a set of cuts that has the highest rejection power but also the lowest identification efficiency. More track quality requirements are applied, cuts on the number of hits in the TRT are introduced, and electron candidates matching a reconstructed photon are now rejected.

### 3.4.2 Muons

There are three main strategies at ATLAS to reconstruct muons [23]: *Standalone Muons*, *Combined Muons* and *Tagged Muons*. For each strategy there are two different algorithms existing: **Staco** and **Muid**.

**Standalone Muons.** Standalone muons are reconstructed by finding tracks in the muon spectrometer which are then extrapolated to the beam line. The two algorithms that perform this extrapolation are called **Muonboy** (for **Staco**) and **Moore** (for **Muid**). They both differ in the way the energy loss in the calorimeter is treated. The advantage of this strategy is that a wide range of  $|\eta|$  can be covered (more than is covered by the Inner Tracker). Yet a disadvantage is that muons having very low momenta might not reach the muon spectrometer and cannot be reconstructed in this case.

**Combined Muons.** Combined Muons are reconstructed by matching standalone muons to the close-by Inner Detector tracks (done by both **Staco** and **Muid**). So the advantage is that both systems, the Inner Detector and the muon spectrometer, are used for measurements that can finally be combined. An important measure of the quality of the match is  $\chi_{match}^2$ , which is defined as the difference between the outer and the inner track vectors weighted by their combined covariant matrix.

Usually combined muons reconstructed with the **Staco** algorithm are used in SUSY analysis.

**Tagged Muons.** Both tagging algorithms (**MuTag** and **MuGirl**) extrapolate Inner Detector tracks (carrying sufficient momenta) to the muon spectrometer and search for nearby hits. If a hit is close enough to the predicted track position, then the track will be reconstructed as a tagged muon.

### 3.4.3 Jets

In ATLAS the so-called anti- $k_T$  algorithm [24] is used for jet reconstruction. Anti- $k_T$  is based upon pair-wise clustering of the initial constituents. The algorithm measures distances between objects: The distance between two objects  $d_{ij}$  is measured as well as the distance  $d_{iB}$  between the object and the beam.  $d_{ij}$  depends on the distance parameter  $\Delta R$  (usually  $\Delta R = 0.4$  or  $\Delta R = 0.6$ ). All values for  $d_{ij}$  and  $d_{iB}$  are computed in a list; If  $d_{ij}$  is the smallest distance, then both objects  $i$  and  $j$  are combined and the list is recomputed. If  $d_{iB}$  is the smallest distance, the object is considered to be a jet and is removed from the list.

# 4. Object and Event Selection in the 2011 Analysis

## 4.1 Event Selection I

The first cut made on event selection level is the GoodRunList (GRL) cut which is only applied to data. It checks if the data samples fulfil basic beam, detector and data-quality requirements otherwise they are not used for physics analysis.

The trigger cut is applied next. Trigger used for data and MC are listed in table 4.1. The electron trigger EF\_e20\_medium requires at least one electron with  $p_T = 20$  GeV or higher, while the muon trigger EF\_mu18 accepts at least one muon with  $p_T = 18$  GeV or higher.

Trigger	Data	MC
electron	EF_e20_medium	EF_e20_medium
muon	EF_mu18	EF_mu18

Table 4.1: Electron and muon trigger for data and MC

## 4.2 Object Definitions and Overlap Removal

There are a certain number of baseline cuts that all ATLAS analyses searching for SUSY (i.e. 0, 1, 2 and multilepton channels) have in common in order to select well-reconstructed electrons, muons and jets fulfilling some basic quality requirements. This first selection is called Object Preselection. After the Object Preselection one has to take into account that the preselected objects do not overlap in order to avoid that an object might be identified twice. Additionally to its “true” particle type it could be mistakenly identified as another object due to an insufficient spatial isolation from the respective one. The spatial isolation  $\Delta R$  is measured in the  $\eta - \phi$  plane and was previously defined by (2.3).

### 4.2.1 Electrons

Baseline electrons are defined as following:

- electrons must be reconstructed with an algorithm `author`<sup>1</sup>:  
 $author = 1$  or  $author = 3$
- Medium identification requirements at preselection level (see section 3.4.1)
- $p_T > 20$  GeV
- $|\eta_{cl}| < 2.47^2$
- Overlap Removal: If the distance between a jet and an electron lies within  $0.2 < |\Delta R(e, jet)| < 0.4$ , the electron is rejected

### 4.2.2 Muons

Baseline muons are defined as following:

- Combined or tagged muons reconstructed with `Staco` algorithm
- Tight identification criteria
- $p_T > 10$  GeV
- $|\eta| < 2.4$
- Each muon must fulfil certain track quality requirements (see section 3.4.2)
- Overlap Removal:  $\Delta R(jet, muon) > 0.4$  otherwise the muon is rejected

### 4.2.3 Jets

The following constraints are made on jets:

- The jet collection `AntiKt4TopoEM` is used: Jets are reconstructed with the anti- $k_T$  algorithm (see section 3.4.3) and calibration is based on the electromagnetic scale<sup>3</sup> with a jet energy scale factor applied (EM+JES method)
- $p_T > 20$  GeV
- $|\eta| < 2.8$
- Overlap Removal:  $\Delta R(e, jet) > 0.2$  otherwise the jet is rejected
- Jet cleaning: If a jet with  $p_T > 20$  GeV is badly reconstructed, the event is discarded

---

<sup>1</sup>This algorithm chooses electrons which were reconstructed by the standard cluster-based algorithm.

<sup>2</sup> $\eta_{cl}$  denotes the calorimeter cluster pseudorapidity.

<sup>3</sup>The electromagnetic (EM) scale provides the correct scale for energy deposited by electromagnetic showers in the ATLAS calorimeter.

## 4.3 Event Selection II

After passing all Object Selection cuts described above, further cuts are made to reduce the SM background.

Events containing cosmic candidates are rejected: Cosmic candidates are muons that satisfy  $d_0 > 2$  mm or  $z_0 > 5$  mm.<sup>4</sup> Furthermore a cut on the primary vertex (interaction point of the  $p - p$  collision) is applied by requiring at least one primary vertex with more than 4 tracks.

Only events which have exactly two leptons are accepted. This results in 3 possible channels differing in flavour ( $ee$ ,  $e\mu$  and  $\mu\mu$ ) and each one being either OS or SS.

The leading  $p_T$  of electrons must be greater than 25 GeV while the leading  $p_T$  of muons has a cut at 20 GeV.

We reject events with an invariant mass  $m_{ll} < 12$  GeV in order to remove low-mass resonances.

At event selection level the leptons are finally required to be *signal* leptons. An isolation cut is introduced which further reduces SM background. For signal electrons the isolation is defined as  $ptcone20/p_T$ <sup>5</sup> and has to be smaller than 0.1. Additionally signal electrons have tight identification criteria (on preselection level only medium electrons were required). Signal muons must fulfil the isolation requirement  $ptcone20 < 1.8$  GeV.

Global event weights are applied to MC events in order to correct the difference in reconstruction efficiencies in data and MC. A further reweighting being necessary for MC is the PileupReweighting which is described next.

### 4.3.1 PileupReweighting

Pileup occurs when multiple simultaneous interactions that are not associated with the primary interaction (and therefore do not belong to the physics event) are recorded by the detector.

There are two different categories of pileup: The “in-time pileup” refers to the number of interactions within the *same* bunch crossing. Whilst the “out-of-time pileup” indicates the overlapping of signals coming from neighbouring bunch crossings. The latter is particularly important for 2011 data taking because the LHC is now running with bunch trains<sup>6</sup> with an in-train bunch separation of 50 ns. The out-of-time pileup effect is therefore not negligible. To account for the pileup conditions the average number of pileup interactions  $\langle\mu\rangle$  is used. To model precisely the pileup conditions on analysis level, each MC event is finally reweighted with a certain factor which depends on the value of  $\langle\mu\rangle$ .

The MC samples used in this 2011 analysis (mc10a) were produced before the official 2011 data taking had started and their simulation is based on a bunch spacing of 75 ns. Small differences between MC and data are therefore to be expected. [25]

<sup>4</sup> $d_0$  is the distance between muon track and primary vertex at the closest point of approach.  $z_0$  is the distance in z-direction with respect to the primary vertex.

<sup>5</sup>The variable  $ptcone20$  is defined as the transverse momentum in a cone with  $\Delta R = 0.2$  around the track of the lepton.

<sup>6</sup>Bunches are grouped in bunch trains.

### 4.3.2 Calculation of Missing Transverse Energy

Due to transverse momentum conservation<sup>7</sup> the transverse momenta of all final state products from a  $p - p$  collision are expected to sum up to zero:

$$\sum \vec{p}_T = \vec{p}_T^{\text{interacting}} + \vec{p}_T^{\text{non-interacting}} = 0 \quad (4.1)$$

If this is not the case and a non-zero vectorial sum of transverse momenta of the reconstructed particles is measured, this indicates the production of non-interacting particles.

The Missing Transverse Energy ( $E_T^{\text{miss}}$ ) [26] is then simply defined as the absolute value of the missing transverse momentum and is calculated as the vectorial sum of the transverse momenta of all reconstructed particles in an event:

$$E_T^{\text{miss}} = \left| \sum \vec{p}_T^{\text{non-interacting}} \right| = \left| - \sum \vec{p}_T^{\text{interacting}} \right|. \quad (4.2)$$

For the use of physics analysis the reconstruction of  $E_T^{\text{miss}}$  in ATLAS includes two contributions: the transverse energy deposits in all calorimeter cells and a muon term<sup>8</sup>. The  $E_T^{\text{miss}}$  components can therefore be expressed by

$$E_x^{\text{miss}} = E_x^{\text{miss,calo}} + E_x^{\text{miss,\mu}}, \quad (4.3)$$

$$E_y^{\text{miss}} = E_y^{\text{miss,calo}} + E_y^{\text{miss,\mu}} \quad (4.4)$$

and the  $E_T^{\text{miss}}$  value can finally be calculated as

$$E_T^{\text{miss}} = \sqrt{(E_x^{\text{miss}})^2 + (E_y^{\text{miss}})^2}. \quad (4.5)$$

A much more detailed description of the reconstruction and calibration of the Missing Transverse Energy can be found in [27] and [28].

For physics analysis use there are different collections of computed Missing Transverse Energy (also abbreviated by MET) available. They differ for instance in energy calibration for the reconstructed objects.

For the work in this thesis *MET\_Simplified20\_RefFinal* is used: The jets are calibrated with the EM+JES method. [26]

### 4.3.3 Signal Regions

As previously stated SS and OS analyses both share the same object and event selection (except the different sign requirement) but the main difference lies in the choice of the signal regions. This is due to the different background compositions that can be found in both channels. Among the backgrounds listed in chapter 3.3, it is clear that the majority of background in the SS channel for instance arises from fake leptons. In the OS channel this contribution is rather small compared to other backgrounds — the main background comes from  $t\bar{t}$  events in this case.

Signal regions are optimised using the mSUGRA  $\tan\beta = 10$  (described in [18]) SUSY model grid. The  $m_0 - m_{1/2}$ <sup>9</sup> plane is divided into two regions: a 2-body and a 3-body region. Depending on the mass difference between squarks and gluinos the following cascade decay substantially differs and produces different signature:

<sup>7</sup>Since the protons are colliding in longitudinal direction the initial sum of the transverse momenta is always zero before the collision takes place.

<sup>8</sup>The muon term includes the momenta of non-isolated muons, i.e. before Overlap Removal and isolation cut.

<sup>9</sup> $m_0$ : common sfermion mass,  $m_{1/2}$ : common gaugino mass

- ( $m_0 \gg m_{1/2}$ ): Squarks decay via a 3-body decay<sup>10</sup> that produces additional jets.
- ( $m_{1/2} \gg m_0$ ): Gluinos decay via a 2-body decay that produces less jets than the 3-body decay. Additionally the LSP carries higher energy as the cascade decay is shorter.

These two regions dividing the  $m_0 - m_{1/2}$  plane justify the existence of more than one signal region. In the 2011 analysis the signal regions (SR) of the dilepton channel are, after optimisations of the signal significance, defined as following [29]:

**OS:**

1. SR-1:  $E_T^{miss} > 250 \text{ GeV}$
2. SR-2: at least 3 jets ( $p_T > 80, 40, 40 \text{ GeV}$ ) and  $E_T^{miss} > 220 \text{ GeV}$
3. SR-3: at least 4 jets ( $p_T > 100, 70, 70, 70 \text{ GeV}$ ) and  $E_T^{miss} > 100 \text{ GeV}$

**SS:**

1. SR-1:  $E_T^{miss} > 100 \text{ GeV}$
2. SR-2: at least 2 jets ( $p_T > 50, 50 \text{ GeV}$ ) and  $E_T^{miss} > 80 \text{ GeV}$

## 4.4 Monte Carlo and Data Samples

The data samples used in this analysis, taken in 2011 at a centre-of-mass energy of 7 TeV, correspond to the runs 178044 to 180614, i.e. from period B2 until the first run from period E. Since the analysis in this thesis is concentrating on dielectron final states, events are taken from the `egamma` stream.

The total integrated luminosity after GRL selection corresponds to  $165 \text{ pb}^{-1}$ . All MC samples (listed in the appendix) used in this analysis are samples from the official mc10a MC production. The SUSYD3PDMaker package version 00-09-30 was used to produce tag p543.

## 4.5 Monte Carlo and Data Comparison

The following plots show comparison plots between collision data taken in 2011 and SM MC for the SS and OS dielectron channel. The data in all these plots corresponds to an integrated luminosity of  $165 \text{ pb}^{-1}$ .

---

<sup>10</sup>Details on the 2-body and 3-body decay can be found in [29].

### 4.5.1 Dielectron OS Channel

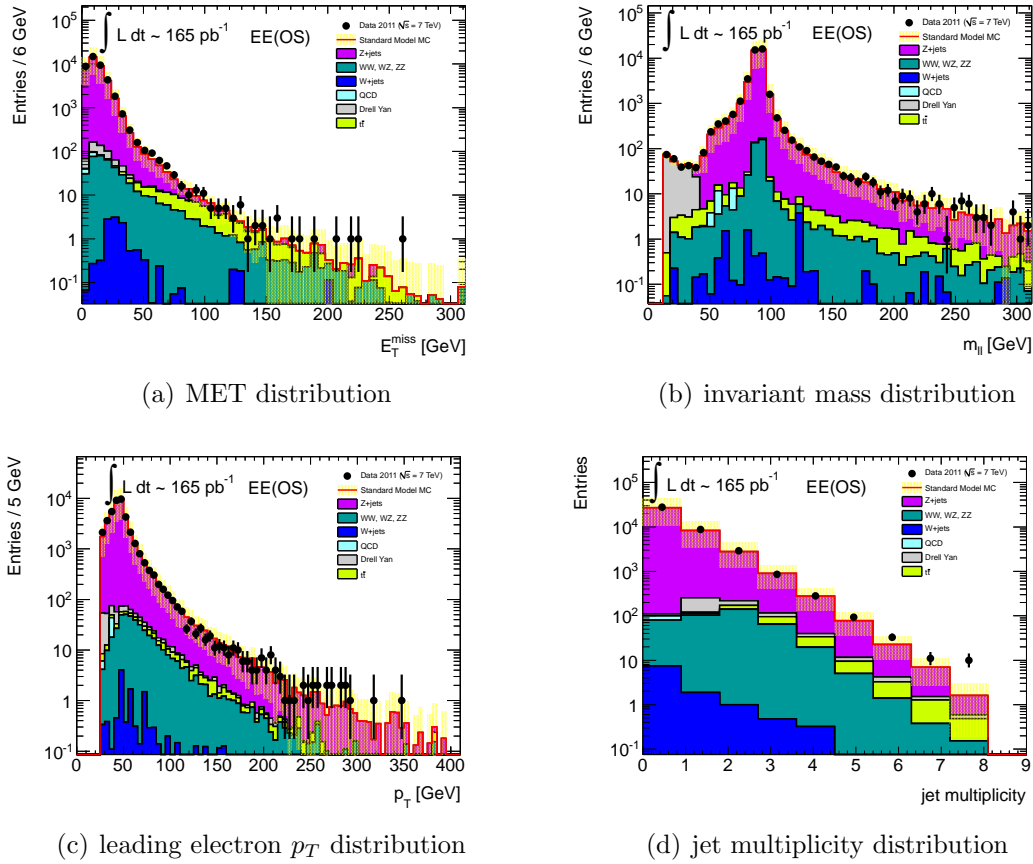


Figure 4.1: MC and data comparison plots for the dielectron OS channel

Figure 4.1 shows the distributions of events with 2 OS electrons in 2011 data (black points) and MC:  $E_T^{miss}$ , invariant mass, leading electron  $p_T$  and jet multiplicity. All MC background processes have been stacked and a very nice agreement between data and MC is observable. Errors on both data and MC are only statistical, no systematic uncertainties have been taken into account. The error on MC is represented by a yellow band while the red line indicates the sum of all SM MC background processes. At an integrated luminosity of  $165 \text{ pb}^{-1}$ , only one data point can be found in OS SR-1 as it is obvious from figure 4.1(a).



## 4.5.2 Dielectron SS Channel

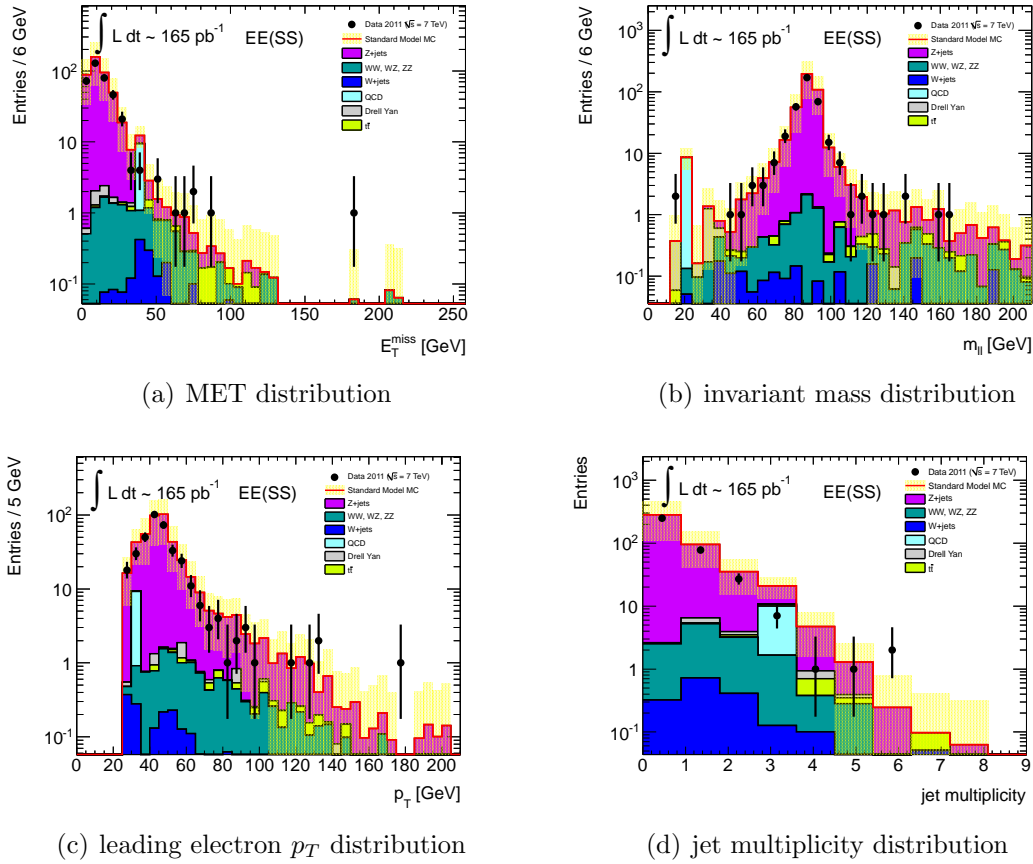


Figure 4.2: MC and data comparison plots for the dielectron SS channel

Figure 4.2 shows the same distributions as figure 4.1 ( $E_T^{miss}$ , invariant mass, leading electron  $p_T$  and jet multiplicity) in 2011 data and MC in the case of two SS final state electrons. Again, there is in general nice agreement between data and MC, though with less statistics — there are less possibilities for decay processes ending up in two SS final state electrons than in two OS ones.

At an integrated luminosity of  $165 \text{ pb}^{-1}$  also a single data point can be found in SS SR-1, as can be seen in figure 4.2(a).



# 5. QCD Background Estimation Using the Matrix Method

The multijet production at the LHC is very large ( $\sigma \sim 9 \cdot 10^9$  pb) but as already mentioned signatures involving jets suffer from rather insufficient modelling [4]. Predictions on the QCD background component should therefore not be based only on MC, but also rely on data-driven estimation techniques.

In the following section a data-driven estimation method will be presented which enables an estimation of the fake lepton contribution in the signal regions of the dilepton channel. The aim of this chapter is to give a compact overview on the method and the way the final estimation is developed. Results that were obtained by applying this method are, however, presented in the following analysis chapter.

## 5.1 Matrix Method

The Matrix method [18] is a method that can be used to estimate the fake lepton contribution in the signal region using collision data. It was first used in ATLAS to measure the fake background to top quark pair production [30]. Yet it can equally be transferred and applied to measure the QCD background in SUSY signal regions containing dilepton final states.

First of all it is necessary to make some important definitions for terms that will be used repeatedly throughout this thesis.

Let's distinguish between two sets (l, T) of leptons that fulfil different identification criteria:

- l: *exclusively* loose lepton, i.e. non-tight
- L: *inclusively* loose lepton, i.e. loose and possibly tight
- T: tight lepton

Furthermore by the use of a subscript F and R, respectively, the following is indicated:

- F: fake lepton, i.e. jet being misidentified as lepton
- R: real lepton, i.e. coming from an electroweak process

The mathematical background concerning the matrix method used in the dilepton channel, rests upon a 4-dimensional matrix. To understand where this matrix and related formula come from, it is useful first to have a look at an application of the method in the *single*-lepton channel.

### 5.1.1 Single-Lepton Channel

The magnitude of QCD background in the single-lepton channel can also be determined using the matrix method. This should briefly be discussed here to infer the formulas for the case of the dilepton estimate.

The number of events with one selected lepton (loose or tight) can be expressed by the following linear combinations:

$$N^{loose} = N_{real}^{loose} + N_{tight}^{loose}, \quad (5.1)$$

$$N^{tight} = r \cdot N_{real}^{loose} + f \cdot N_{tight}^{loose}. \quad (5.2)$$

$r$  indicates the probability that a real loose lepton passes tight criteria while  $f$  represents the probability that a fake loose lepton passes tight criteria. Both probabilities are defined by

$$r = \frac{N_{real}^{tight}}{N_{real}^{loose}} \quad (5.3)$$

and

$$f = \frac{N_{fake}^{tight}}{N_{fake}^{loose}}. \quad (5.4)$$

By measuring these two probabilities one can derive the number of events with a fake lepton that passes tight selection criteria simply by solving the system of equations (5.1) and (5.2):

$$N_{fake}^{tight} = \frac{f}{r - f} (r \cdot N^{loose} - N^{tight}). \quad (5.5)$$

### 5.1.2 Dilepton Channel

The system of equations (5.1) and (5.2) could easily be expressed by a single equation containing a 2-by-2 matrix. Now that we are proceeding with final states containing two leptons, it is possible to extend this 2-dimensional matrix to a 4-dimensional one which accounts for the presence of a second lepton:

$$\begin{bmatrix} N_{TT} \\ N_{Tl} \\ N_{lT} \\ N_{ll} \end{bmatrix} = \begin{bmatrix} rr & rf & fr & ff \\ r(1-r) & r(1-f) & f(1-r) & f(1-f) \\ (1-r)r & (1-r)f & (1-f)r & (1-f)f \\ (1-r)(1-r) & (1-r)(1-f) & (1-f)(1-r) & (1-f)(1-f) \end{bmatrix} \begin{bmatrix} N_{RR}^{LL} \\ N_{RF}^{LL} \\ N_{FR}^{LL} \\ N_{FF}^{LL} \end{bmatrix} \quad (5.6)$$

On the left-hand side a vector consisting of elements denoting events with 2 tight leptons ( $N_{TT}$ ), one tight and one exclusively loose lepton ( $N_{Tl} = N_{lT}$ ) and two

exclusively loose leptons ( $N_{ll}$ ) appears. On the right-hand side there is an analogous vector containing now real-real, real-fake and fake-fake events which are passing preselection cuts (therefore the additional index  $LL$  is printed).

This formula relates the *true* composition of the sample in terms of real and fake leptons with its *observable* composition in terms of loose and tight leptons.

As we do not distinguish between both leptons the 4-by-4 matrix can be reduced to a simpler 3-by-3 matrix. In the end the wanted composition of the signal sample, i.e. the number of events with two real leptons ( $N_{RR}$ ), one real and one fake lepton ( $N_{RF} = N_{FR}$ ) and two fake leptons ( $N_{FF}$ ) in the final states, is derived by a simple inversion of the matrix (5.6).

All elements of the matrix are functions of the variables  $r$  and  $f$ . These variables can be identified with the single lepton efficiency  $r$  and the single fake rate  $f$ . The lepton efficiency  $r$  is the probability that a *real* preselected lepton passes tight criteria. Whilst the fake rate  $f$  denotes the probability that a *fake* preselected lepton passes tight criteria.

To calculate these probabilities one first has to determine the dilepton efficiencies  $\epsilon_{real}$  and  $\epsilon_{fake}$ :

$$\epsilon_{real} = \frac{N_{TT}}{N_{LT}} = \frac{N_{TT}}{N_{IT} + N_{TT}} \quad (5.7)$$

$$\epsilon_{fake} = \frac{N_{IT}}{N_{IL}} = \frac{N_{IT}}{N_{ll} + N_{IT}}. \quad (5.8)$$

These two efficiencies are then converted into the one lepton (real and fake) efficiencies  $r$  and  $f$  by

$$r = \frac{2 \cdot \epsilon_{real}}{1 + \epsilon_{real}} \quad (5.9)$$

$$f = \frac{\epsilon_{fake}}{2 - \epsilon_{fake}}. \quad (5.10)$$

Therefore determining the fake rate  $f$  and lepton efficiency  $r$  is carried out by counting the event numbers, belonging to the various compositions of events containing loose and tight leptons, respectively. The fake rate  $f$  is measured in a control region containing mostly QCD events, while the real efficiencies  $r$  are extracted from a real lepton control region. Having this information, the matrix can eventually be inverted and the fake estimation afterwards be derived.

Solving the system of equations gives (analogously to equation (5.5) in the case of one final state lepton):

$$N_{RR}^{LL} = \frac{[N_{TT}(1-f)^2 - N_{IT}f(1-f) + N_{ll}f^2]}{(r-f)^2} \quad (5.11)$$

$$N_{RF}^{LL} = \frac{[-2N_{TT}(1-r)(1-f) + N_{IT}(r+f-2rf) - 2rfN_{ll}]}{(r-f)^2} \quad (5.12)$$

$$N_{FF}^{LL} = \frac{[N_{TT}(1-r)^2 - r(1-r)N_{IT} + r^2N_u]}{(r-f)^2} \quad (5.13)$$

Finally the true composition of the signal sample can now be derived in terms of real and fake leptons using the relations

$$N_{RR}^{TT} = N_{RR}^{LL} \cdot r^2 \quad (5.14)$$

$$N_{RF}^{TT} = N_{RF}^{LL} \cdot r f \quad (5.15)$$

$$N_{FF}^{TT} = N_{FF}^{LL} \cdot f^2 \quad (5.16)$$

where  $N_{RR}^{TT}$  are 2 signal (=tight) leptons being estimated as a real-real event,  $N_{RF}^{TT}$  estimated as a real-fake event and finally in the case of  $N_{FF}^{TT}$  both leptons are estimated to be fake leptons.

# 6. QCD Background Estimation with 2011 Data

The aim of this work is to give an estimation of the fake background contribution in the various signal regions of the dilepton channel, using the matrix method.

## 6.1 Loose / Tight Definitions for Electrons

In order to calculate fake rates and real efficiencies it is first necessary to define two different sets of identification criteria: loose and tight electrons<sup>1</sup>.

**Tight electrons.** Tight electrons are signal electrons as defined in 4.3. They have an isolation cut at  $ptcone20/p_T < 0.1$  and are required to fulfil tight identification criteria (see section 3.4.1).

**Loose electrons.** The sample of loose electrons is defined by relaxing the identification criteria in order to enhance the contribution of electrons coming from QCD processes: The isolation cut is loosened to  $ptcone20/p_T < 4$ . Loose electrons are required to fulfil only *medium* electron identification criteria.

After defining these two samples, the numbers of events with respect to tight - tight, exclusively loose - tight and exclusively loose - exclusively loose electron pairs<sup>2</sup> need to be counted in the corresponding signal regions.

## 6.2 Choice of Control Regions

In order to calculate the real efficiency  $r$  and the fake rate  $f$  using the formulas (5.7) and (5.8) one has to define a fake and a real lepton control region. Fake control regions are dominated by fake electrons and are used to obtain the probability that

---

<sup>1</sup>The definition of loose and tight electrons was taken from a group in Oslo also working on the field of fake background estimation

<sup>2</sup>It is important to differ between exclusively loose (l), i.e. non-tight and inclusively loose (L) electrons as emphasized in chapter 5.

a fake loose lepton passes tight criteria. Therefore these regions are also called QCD control regions.

The probability of a real loose lepton passing tight criteria can be extracted from a real lepton control region, consisting mainly of real electrons. Since this region is chosen to contain events coming from  $Z$  events it is often referred to as  $Z$ -control region.

One basic requirement needed by the matrix method to provide precise results, is that both efficiencies should depend as little as possible on the event topology. After they are determined in control regions the efficiencies have to be applied in the signal region. This only makes sense if they do not substantially differ, for instance the composition of the fake control region should be similar to the fake composition in the signal region. The real efficiency obtained from a  $Z$ -control region is required to resemble the real efficiency for leptons originating also from other processes, e.g.  $W$ +jets.

Another two main aspects have to be considered before choosing a certain control region that is used to extract efficiencies from: On the one hand the choice of a control region has to rely on its purity — a fake control region should be mainly dominated by fake electrons, whereas a real control region should be dominated by real electrons. On the other hand one needs of course reasonable statistics to work with. Little statistics is a problem that usually fake control regions are affected with because the probability that two electrons are fake is very small.

The purity of a region is defined by

$$\text{Purity} = \frac{N_{data}^{dilepton} - N_{non-QCD}^{dilepton}}{N_{data}^{dilepton}} \sim \frac{N_{QCD}^{dilepton}}{N_{data}^{dilepton}} \quad (6.1)$$

Hence the purity measures the contamination of a region as the amount of non-QCD MC processes contributing to this region. Regions having high purities are therefore dominated by fake events whilst regions with very low purities consist mainly of real electrons.

A selection of various control regions and respective statistics is shown in table 6.1.

Each region is defined by slightly different cuts. All fake regions listed here, denoted by  $fx$ , are  $SS$  regions, i.e. the electrons must have the same charge.  $Z$  means that a  $Z$ -veto is applied, i.e. events lying within the narrow  $Z$  mass peak defined by  $\Delta m(ll, Z) < 5 \text{ GeV}$ , are discarded. This is done because electrons contributing to this region mainly come from  $Z$  decay and are therefore real electrons<sup>3</sup>. Real electrons contributing to the fake control region worsen the purity and therefore artificially push the fake rate up. All regions listed in the table were evaluated with and without a  $Z$ -veto applied. By comparing two corresponding regions, one can see that the fake rates are higher for the regions without any  $Z$ -veto.

The fact that these regions are contaminated by a non-negligible amount of non-QCD events, is also reflected in the value of the respective purities for exclusively loose - exclusively loose and exclusively loose - tight electron pairs. Regions having higher fake rates (e.g. the ones without  $Z$ -veto) have at the same time lower purities

<sup>3</sup>As we are working here with  $SS$  regions the  $Z$  contribution comes from charge misidentification.



Region	N(l)	N(lT)	N(TT)	Purity (l)	Purity(lT)	Rates ( $r$ or $f$ )
f1: $N_{jet} \geq 1$	485	427		0.754	-0.03	0.306
f2: $N_{jet} \geq 2$	196	179		0.821	-0.12	0.313
f3: $N_{jet} \geq 1, Z$	401	199		0.850	0.143	0.199
f4: $N_{jet} \geq 2, Z$	162	90		0.897	0.22	0.217
f5: $E_T^{miss} < 10$	280	466		0.581	-1.08	0.454
f6: $E_T^{miss} < 20$	661	874		0.678	-0.11	0.398
f7: $E_T^{miss} < 60$	1003	1125		0.695	-0.12	0.359
f8: $E_T^{miss} < 10, Z$	197	114		0.85	0.15	0.224
f9: $E_T^{miss} < 20, Z$	492	253		0.890	0.17	0.205
f10: $E_T^{miss} < 60, Z$	770	388		0.863	0.05	0.201
f11: $N_{jet} \geq 1, E_T^{miss} < 20$	249	239		0.775	-0.08	0.324
f12: $N_{jet} \geq 2, E_T^{miss} < 20$	87	87		0.827	0.014	0.333
f13: $N_{jet} \geq 3, E_T^{miss} < 20$	28	23		0.962	0.048	0.291
<b>f14: <math>N_{jet} \geq 1, E_T^{miss} &lt; 20, Z</math></b>	<b>201</b>	<b>84</b>		<b>0.911</b>	<b>0.149</b>	<b>0.173</b>
f15: $N_{jet} \geq 1, E_T^{miss} < 40, Z$	359	143		0.876	0.09	0.166
f16: $N_{jet} \geq 2, E_T^{miss} < 20, Z$	70	33		0.942	0.150	0.202
f17: $N_{jet} \geq 3, E_T^{miss} < 20, Z$	25	9		0.958	0.33	0.152
r: OS, $85 < m_{ll} < 96$ GeV		14545	40811			0.848

Table 6.1: Control region statistics (all fake regions are SS regions)

due to the real electron contribution. For some of the exclusively loose - tight events the purities become negative. This comes from a lack of statistics in this region. Another striking thing are the very low purity values for this set of electron pairs. The main reason for this contamination lies of course in the presence of the tight electron which is in most cases indeed a real electron.

Before proceeding we now choose the best suited control region to further work with. For the background estimation presented here, region f14 was selected: It is defined by the cuts  $SS, N_{jet} \geq 1, E_T^{miss} < 20, Z$  and the fake rate determined is  $f = 0.173$ . It is considered to be the most appropriate set because region f17, for instance showing the best purity for both sets of electrons, suffers from a lack of statistics. Region f15 on the other hand, showing quite more statistics, has indeed a worse purity. Eventually one has to find a compromise between both, this is why region f14 is preferred.

In case of the real lepton control region a natural choice is to select OS events within a narrow  $Z$  mass window: The invariant mass  $m_{ll}$  has to lie within the range  $85 < m_{ll} < 96$  GeV, called  $Z$ -control region. The real efficiency is evaluated as  $r = 0.848$ . The  $Z$ -control region is not suffering from a lack of statistics. Due to the high ratio of real electrons and sufficient statistics it is not necessary to further optimise the cuts defining this control region.

### 6.3 Real Electron Control Region

Figure 6.1 shows two validation plots for the real electron control region previously defined. Validation plots are useful to check the origin (with respect to real and fake) of the electron pairs present in this region.

The left plot shows the invariant mass distribution for OS tight - tight electron pairs whilst the right validation plot shows the invariant mass distribution for OS exclusively loose - tight electron pairs. From both plots it becomes obvious that for the region  $85 < m_{ll} < 96$  GeV the vast majority of electrons comes from Z decay and is therefore real.

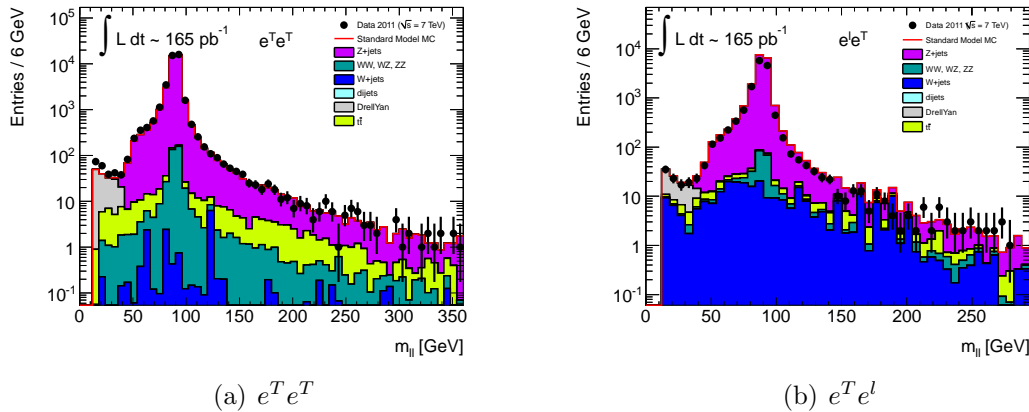
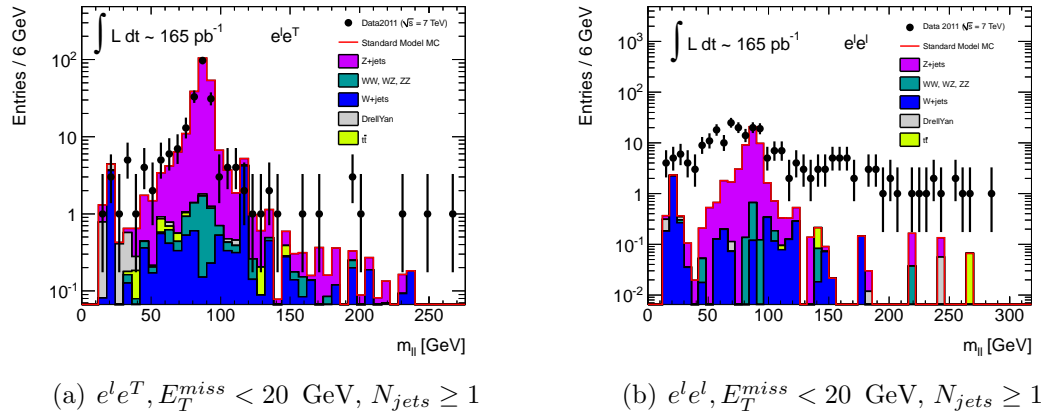


Figure 6.1: Validation plots for  $e^T e^T$  and  $e^L e^T$  pairs

### 6.4 Fake Control Region

Two validation plots for the QCD control region f14 ( $N_{jet} \geq 1$ ,  $E_T^{miss} < 20$ , Z) before applying a Z-veto are depicted in figure 6.2. LHC data and non-QCD SM contributions are shown. The plot on the left shows again the invariant mass distribution for exclusively loose - tight electron pairs. One can see a big contribution coming from Z decay (due to charge misidentification). This circumstance is reflected in the low purity values derived for  $e^L e^T$  pairs. However, the validation plot for exclusively loose - exclusively loose electron pairs shown on the right proves that this region is well-selected and dominated by fakes since an excess of data compared to non-QCD SM background is visible. Applying a Z-veto will further remove the vast majority of real electrons and raise the purity. This can be seen in table 6.1 by comparing region f14 with f11, the latter without any Z-veto applied. f11 has a purity value of 0.775 for exclusively loose - exclusively loose electron pairs which is raised to 0.911 for region f14 including a Z-veto.

Figure 6.2: Validation plots for  $e^l e^T$  and  $e^l e^l$  pairs

## 6.5 Real Efficiencies

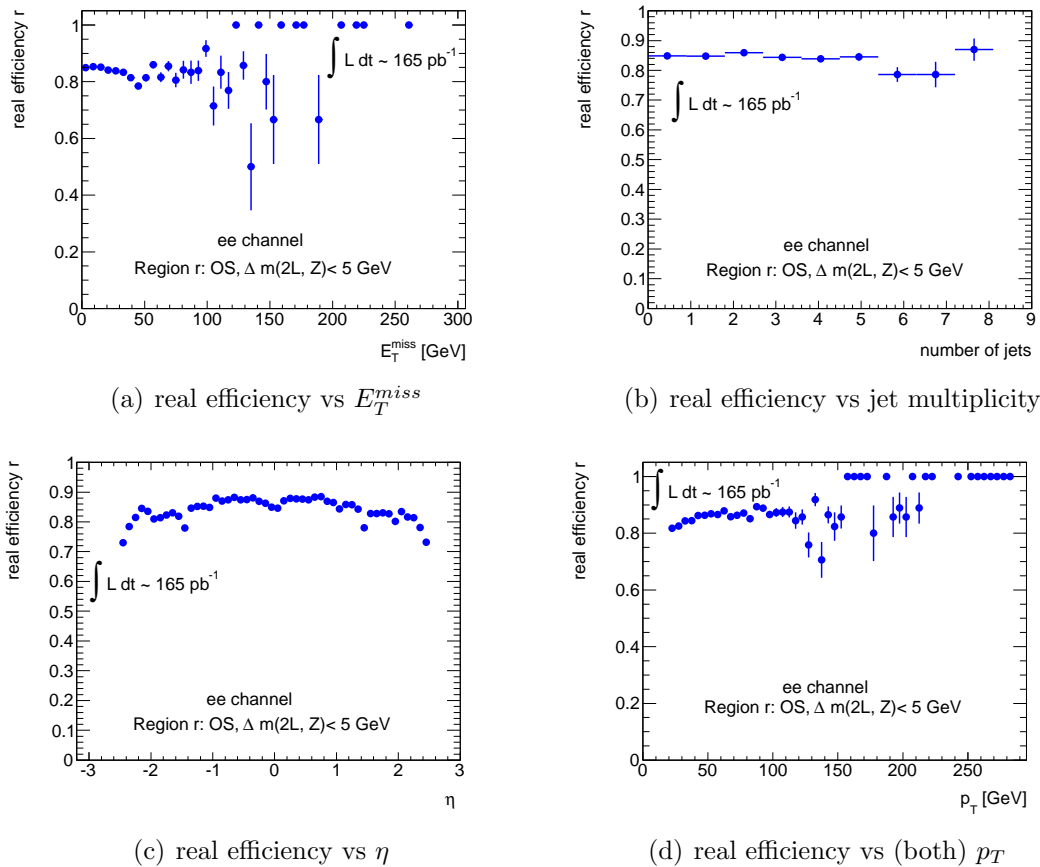


Figure 6.3: Real efficiency extracted from the real electron control region plotted as a function of different event variables

Real efficiencies extracted from the Z-control region are plotted in figure 6.3 as a function of different event variables for an integrated luminosity of  $165 \text{ pb}^{-1}$ . The plots show dependencies against  $E_T^{miss}$  in 6.3(a), jet multiplicity in 6.3(b),  $\eta$  in 6.3(c) and the leptons  $p_T$  in 6.3(d). The average real efficiency is  $r = 0.848$  (see table 6.1). In general, the efficiencies are in regions with sufficient statistics rather stable. In some figures a few bins have a real efficiency of 1. In this case the bin contains only

one single tight - tight event which results in  $r = 1$  using (5.7) and (5.9). All errors are statistical.

## 6.6 Fake Rates

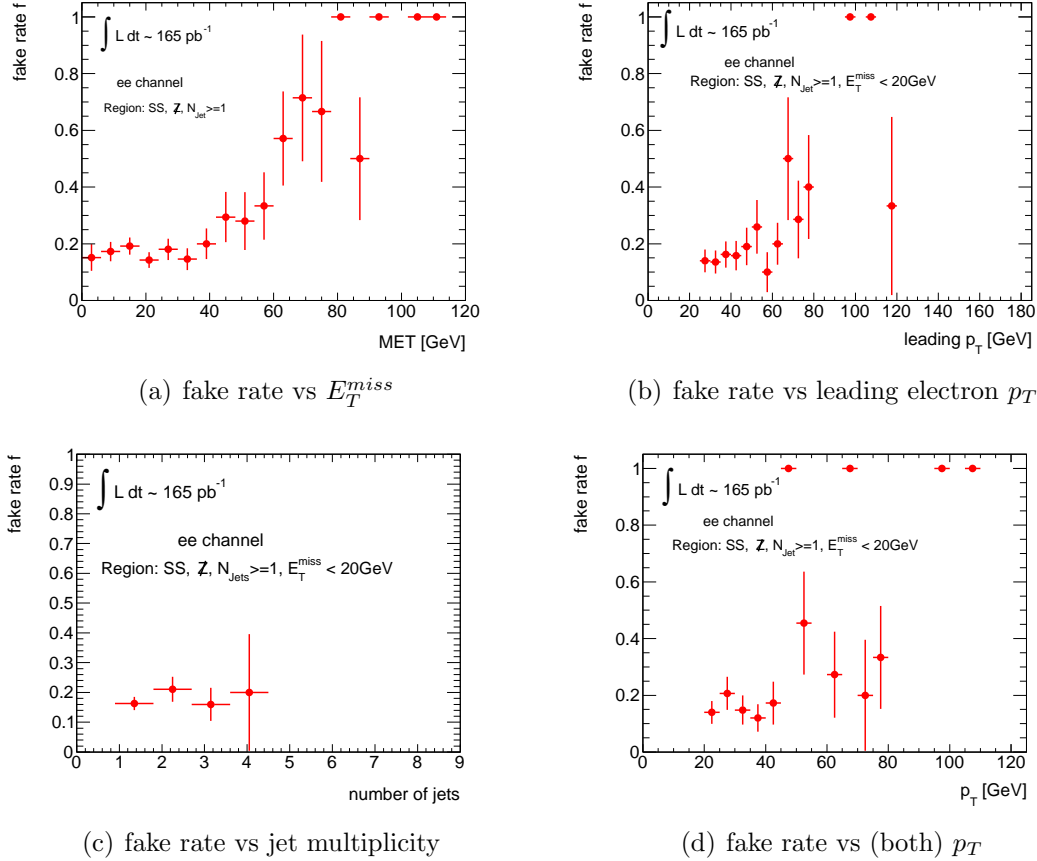


Figure 6.4: Electron fake rates from the selected QCD control region f14 plotted as a function of different event variables

Fake-rates obtained from the SS QCD control region f14, defined by  $N_{jet} \geq 1$ ,  $E_T^{miss} < 20$ ,  $Z$  are plotted for  $165 \text{ pb}^{-1}$  against different event variables in figure 6.4. The fake rate is plotted versus  $E_T^{miss}$  in figure 6.4(a), the leading electron  $p_T$  in figure 6.4(b), jet multiplicity in 6.4(c) and both  $p_T$  values of the event in 6.4(d). The average fake rate extracted from region f14 is  $f = 0.173$ . One can infer from all figures the fake dependencies are fluctuating around the average fake rate a lot more than the real efficiencies do. This is due to lower statistics in the fake control regions. The fake rate increases at large  $E_T^{miss}$  and  $p_T$ .

Again all errors are statistical and fake rates of exactly 1 appear in bins where only one exclusively loose - tight event is present.

## 6.7 Results

Having derived fake rates and real efficiencies, the fake background estimation can finally be concluded by simply counting the number of tight - tight, exclusively loose - tight and exclusively loose - exclusively loose events in the respective signal regions (defined in chapter 4.3.3). Then using the formulas (5.14) - (5.16) the real-real, real-fake and fake-fake contributions can be estimated. In the following subsections this final estimation is shown for all 5 signal regions of the dilepton channel.

### 6.7.1 OS Signal Region - 1

In this section the results derived for the fake background estimation using the matrix method will be explained exemplary for the OS signal region 1 which is defined by an  $E_T^{miss} > 250$  GeV cut.

Figure 6.5 shows the  $E_T^{miss}$  distribution at an integrated luminosity of  $165 \text{ pb}^{-1}$  in a region where no jet requirement is made (all other signal regions except SS SR-1 have certain jet requirements). MC background is plotted without QCD MC contribution, instead the results of derived fake estimation are shown. Dark-blue squares denote events with two estimated real electrons, i.e. the number of real tight events  $N_{RR}^{TT}$  calculated using (5.14). Turquoise triangles correspond to events with one real tight and one fake tight electron, i.e.  $N_{RF}^{TT}$  derived from (5.15). The contribution from events where both electrons are estimated as fake tight electrons, defined by  $N_{FF}^{TT}$  (5.16), is depicted by orange triangles. Finally, red stars indicate the number of dilepton events where at least one electron is estimated to be a fake electron:  $N(FF) + N(RF)$ .

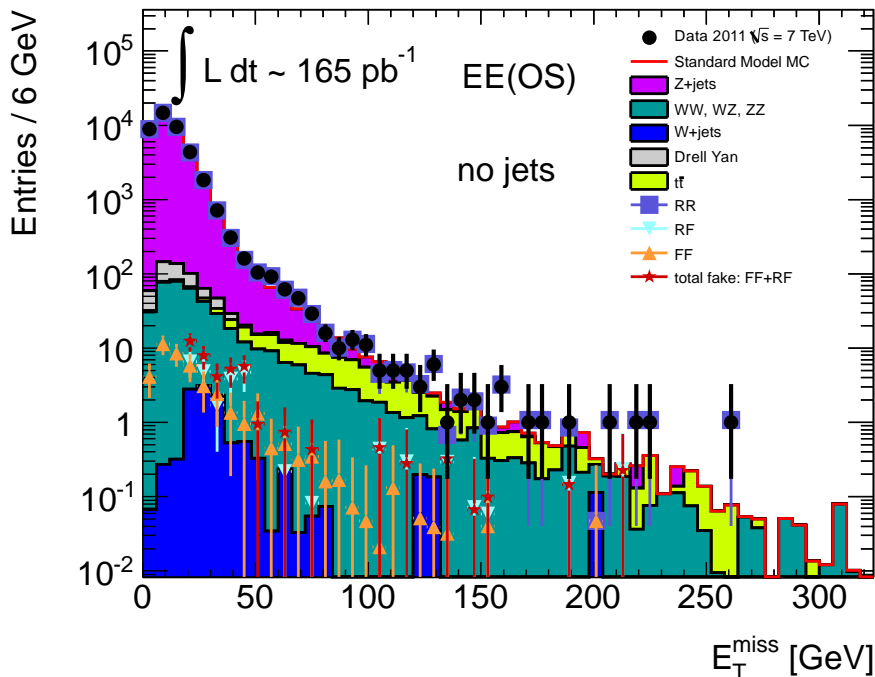


Figure 6.5: Dielectron OS  $E_T^{miss}$  distribution without jet requirement

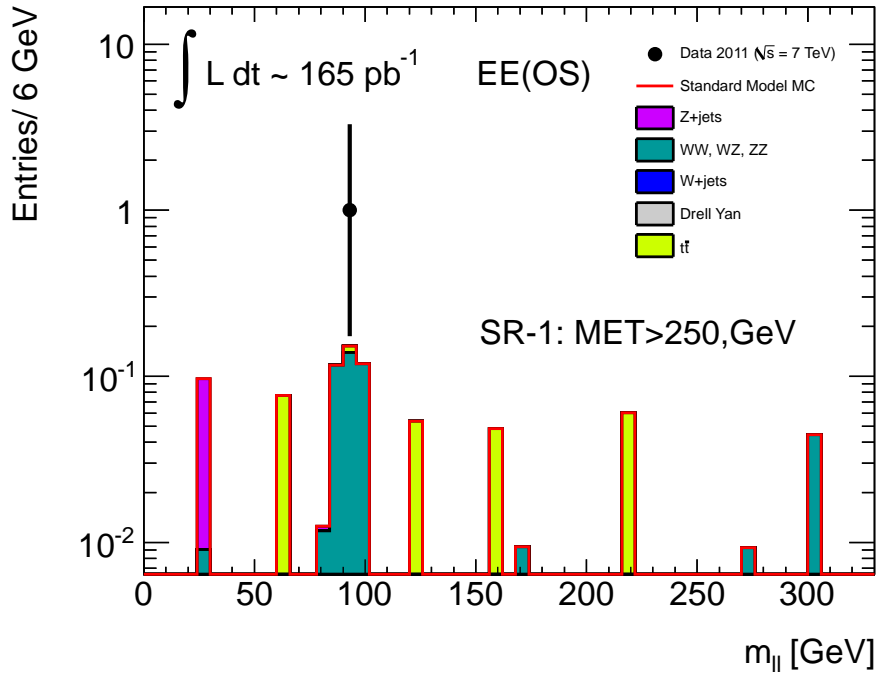


Figure 6.6: Invariant mass distribution in OS SR-1

Bin [GeV]	N(TT)	N(IT)	N(ll)	f	r	N(RR)	N(RF)	N(FF)
0-30	37365	13150	1791	0.173	0.848	37448.2	-113.2	30.0
30-60	3126	1273	322	0.173	0.848	3102.1	14.7	9.2
60-90	246	94	47	0.173	0.848	246.5	-2.3	1.8
90-120	44	17	11	0.173	0.848	44.18	-3.24	0.44
120-150	17	7	3	0.173	0.848	16.9	-0.01	0.1
150-180	7	2	1	0.173	0.848	7.2	-0.2	0.0
180-210	2	1	1	0.173	0.848	2.0	0.0	0.0
210-240	3	1	0	0.173	0.848	3.0	0.0	0.0
240-270	1	0	0	0.173	0.848	1.1	-0.1	0.0
Overflow	0	0	0	0.173	0.848	0.0	0.0	0.0

Table 6.2: Binwise fake/real estimation for  $E_T^{miss}$  distribution in OS channel without jet requirement

Figure 6.6 shows the invariant mass distribution containing only events with  $E_T^{miss} > 250$  GeV. In this signal region only one data point can be found. In table 6.2 the fake background estimation is given in steps of 30 GeV in  $E_T^{miss}$ . The table lists for each 30 GeV step the respective number of tight-tight events  $N(TT)$ , exclusively loose - tight events  $N(IT)$  and exclusively loose - exclusively loose events  $N(LL)$ . The fake rate  $f$  and real efficiency  $r$  are the same for each bin since they correspond to the integrated rate and efficiency previously determined from control regions in section 6.2. Using the formulas quoted above one can calculate now the number of electrons for each bin in terms of estimated real-real ( $N(RR)$ ), real-fake ( $N(RF)$ ) and fake-fake ( $N(FF)$ ) events. When comparing the *observed* event number  $N(TT)$  with the estimated *real* numbers in the right column, the bin [240-270] GeV is estimated to contain one real-real event. Hence the conclusion is that the only data point present in OS SR-1, is estimated to be a real-real event.

The presentation of the results for the signal regions following is analogous and a detailed description will therefore not be repeated.

### 6.7.2 OS Signal Region - 2

The OS SR-2 is defined by the presence of at least 3 jets with  $p_T > 80, 40, 40$  GeV and  $E_T^{miss} > 220$  GeV.

We can conclude that the only data point present in this region is estimated to be a real-real event:  $N(RR)=1.1$  (see table 6.3).

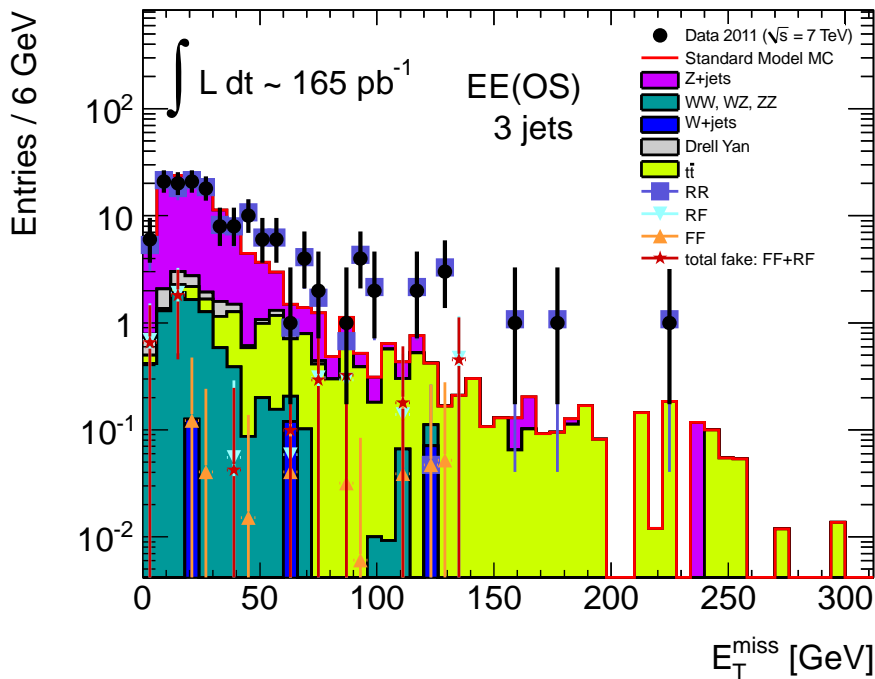


Figure 6.7: Dielectron OS  $E_T^{miss}$  distribution,  $N_{jets} \geq 3$

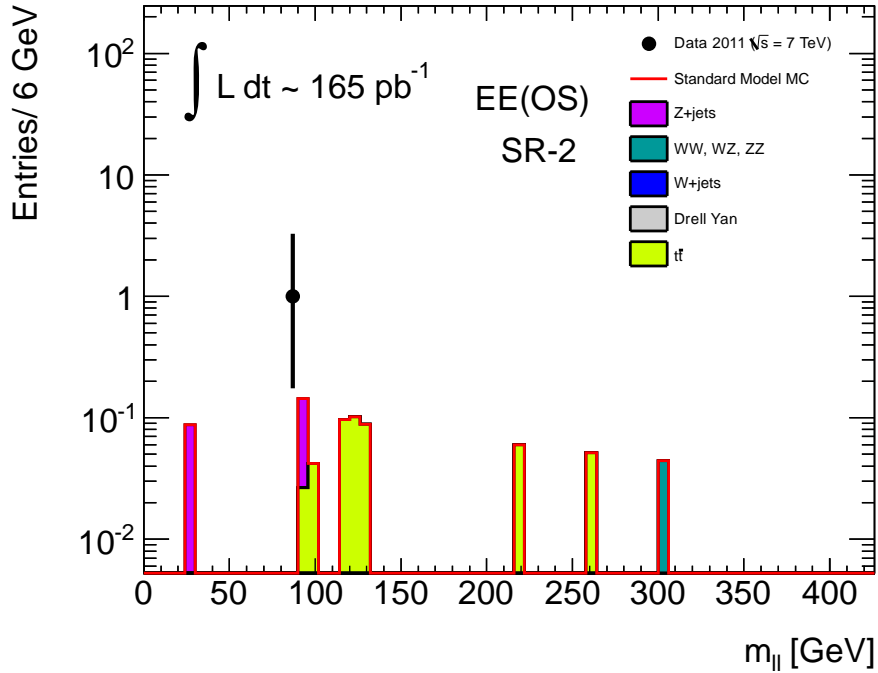


Figure 6.8: Invariant mass distribution in OS SR-2

Bin [GeV]	N(TT)	N(IT)	N(II)	f	r	N(RR)	N(RF)	N(FF)
0-30	68	31	3	0.173	0.848	66.5	1.5	0.0
30-60	50	10	1	0.173	0.848	51.8	-1.8	0.0
60-90	13	5	1	0.173	0.848	13.0	0.0	0.0
90-120	7	3	2	0.173	0.848	7.0	0	0.1
120-150	5	2	2	0.173	0.848	5.0	-0.1	0.1
150-180	1	0	0	0.173	0.848	1.1	-0.1	0.0
180-210	1	0	0	0.173	0.848	1.1	-0.1	0.0
210-240	1	0	0	0.173	0.848	1.1	-0.1	0.0
240-270	0	0	0	0.173	0.848	0	0	0
Overflow	0	0	0	0.173	0.848	0	0	0

Table 6.3: Binwise fake/real estimation for  $E_T^{miss}$  distribution in OS channel with  $N_{jet} \geq 3$  requirement

### 6.7.3 OS Signal Region - 3

The OS SR-3 is defined by the presence of at least 4 jets with  $p_T > 100, 70, 70, 70$  GeV and  $E_T^{miss} > 100$  GeV. In this region, there is no data point present.



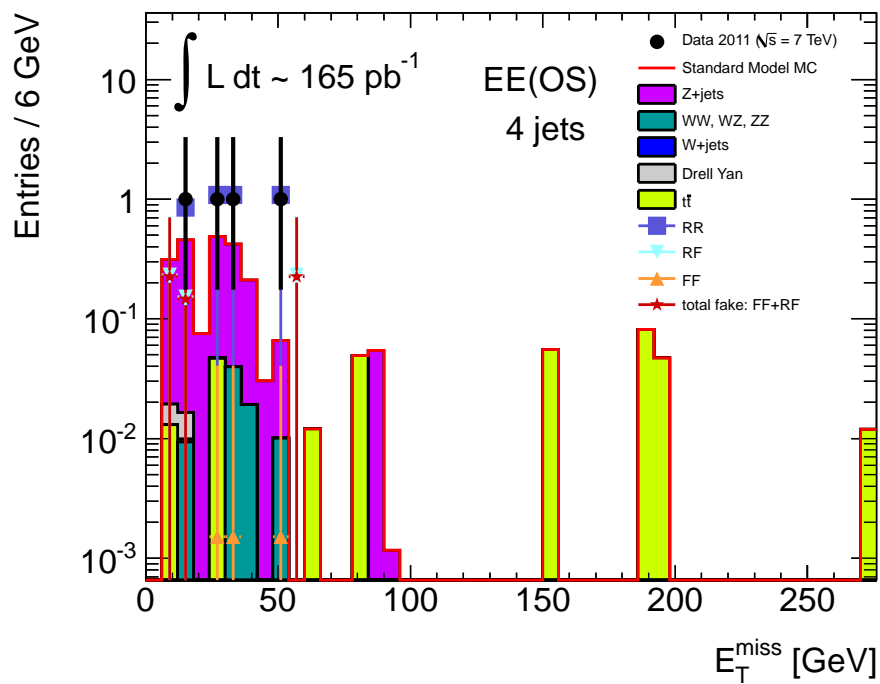
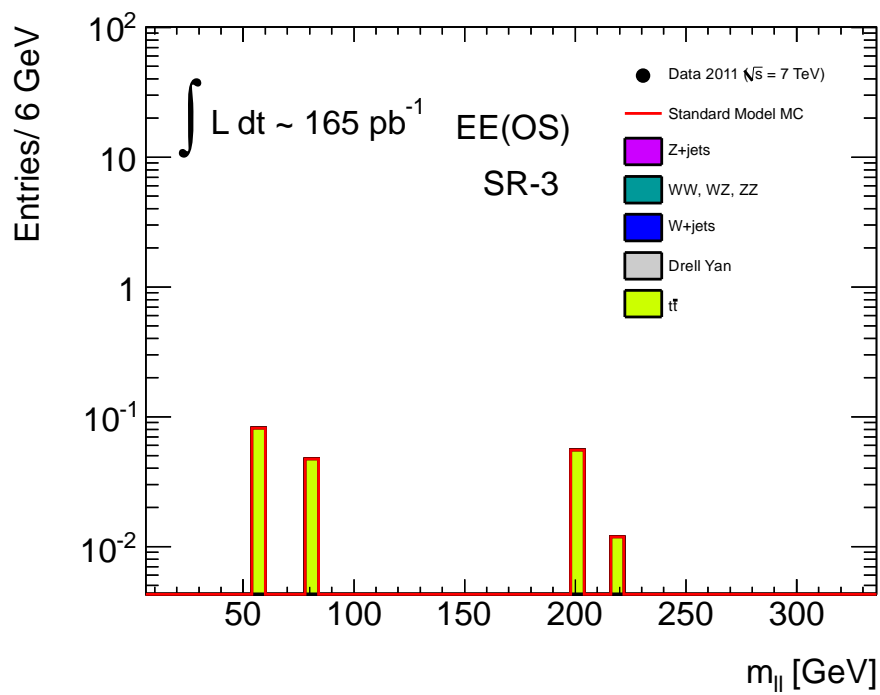
Figure 6.9: Dielectron OS  $E_T^{\text{miss}}$  distribution  $N_{\text{jets}} \geq 4$ 

Figure 6.10: Invariant mass distribution in OS SR-3

Bin [GeV]	N(TT)	N(IT)	N(ll)	f	r	N(RR)	N(RF)	N(FF)
0-30	1	2	0	0.173	0.848	0.6	0.4	0.0
30-60	3	0	0	0.173	0.848	3.2	-0.2	0.0
60-90	0	1	0	0.173	0.848	-0.2	0.2	0.0
90-120	0	0	0	0.173	0.848	0	0	0
120-150	0	0	0	0.173	0.848	0	0	0
150-180	0	0	0	0.173	0.848	0	0	0
180-210	0	0	0	0.173	0.848	0	0	0
210-240	0	0	0	0.173	0.848	0	0	0
240-270	0	0	0	0.173	0.848	0	0	0
Overflow	0	0	0	0.173	0.848	0	0	0

Table 6.4: Binwise fake/real estimation for  $E_T^{miss}$  distribution in OS channel with  $N_{jet} \geq 4$  requirement

### 6.7.4 SS Signal Region - 1

The SS SR-1 is defined by an  $E_T^{miss} > 100$  GeV cut.

We can conclude that the only data point present in this region is estimated to be a real-real event:  $N(RR)=1.0$  (see table 6.6).

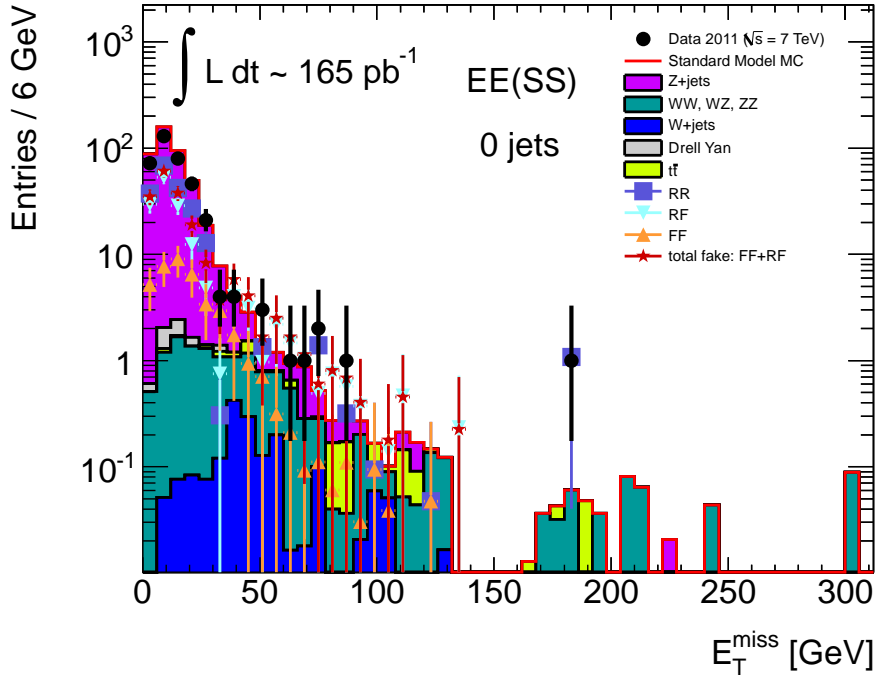


Figure 6.11: Dielectron SS  $E_T^{miss}$  distribution without jet requirement

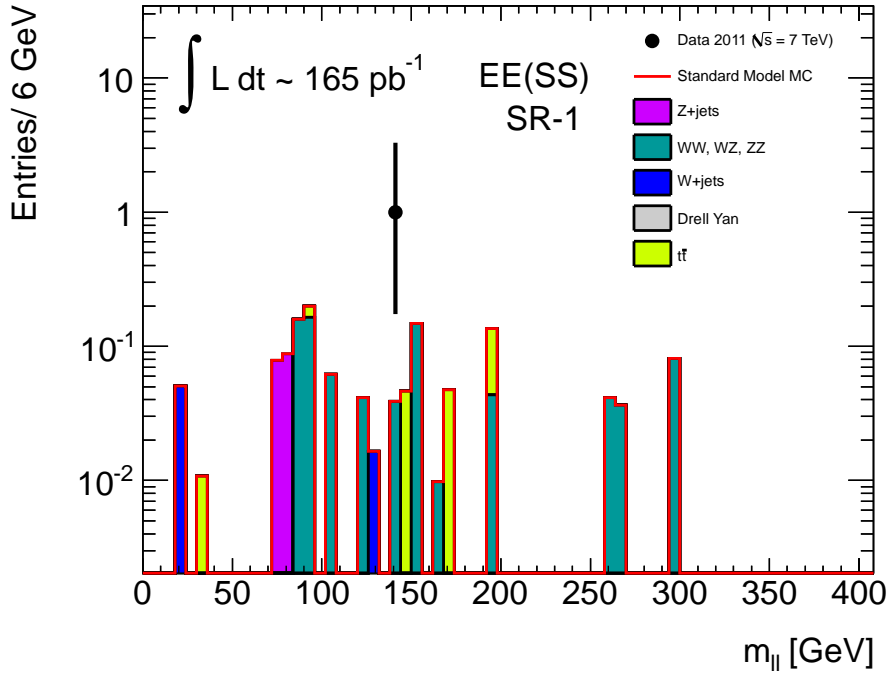


Figure 6.12: Invariant mass distribution in SS SR-1

Bin [GeV]	N(TT)	N(IT)	N(ll)	f	r	N(RR)	N(RF)	N(FF)
0-30	327	948	760	0.173	0.848	174.8	123.8	28.4
30-60	32	164	234	0.173	0.848	8.6	13.7	9.7
60-90	4	36	23	0.173	0.848	-2.7	5.9	0.8
90-120	1	9	7	0.173	0.848	-0.6	1.4	0.3
120-150	0	1	1	0.173	0.848	-0.2	0.1	0.0
150-180	1	0	0	0.173	0.848	1.0	0	0
180-210	0	0	0	0.173	0.848	0	0	0
210-240	0	0	0	0.173	0.848	0	0	0
240-270	0	0	0	0.173	0.848	0	0	0
Overflow	0	0	0	0.173	0.848	0	0	0

Table 6.5: Binwise fake/real estimation for  $E_T^{miss}$  distribution in SS channel without jet requirement

### 6.7.5 SS Signal Region - 2

The SS SR-2 is defined by the presence of at least 2 jets with  $p_T > 50, 50$  GeV and  $E_T^{miss} > 80$  GeV. In this region, there is no data point present.

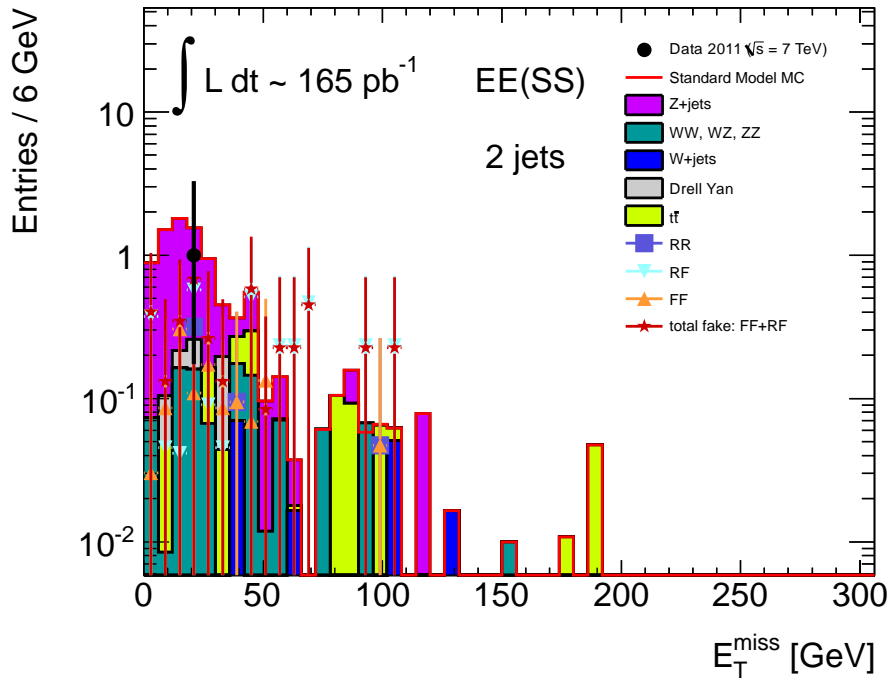


Figure 6.13: Dielectron SS  $E_T^{\text{miss}}$  distribution,  $N_{\text{jets}} \geq 2$

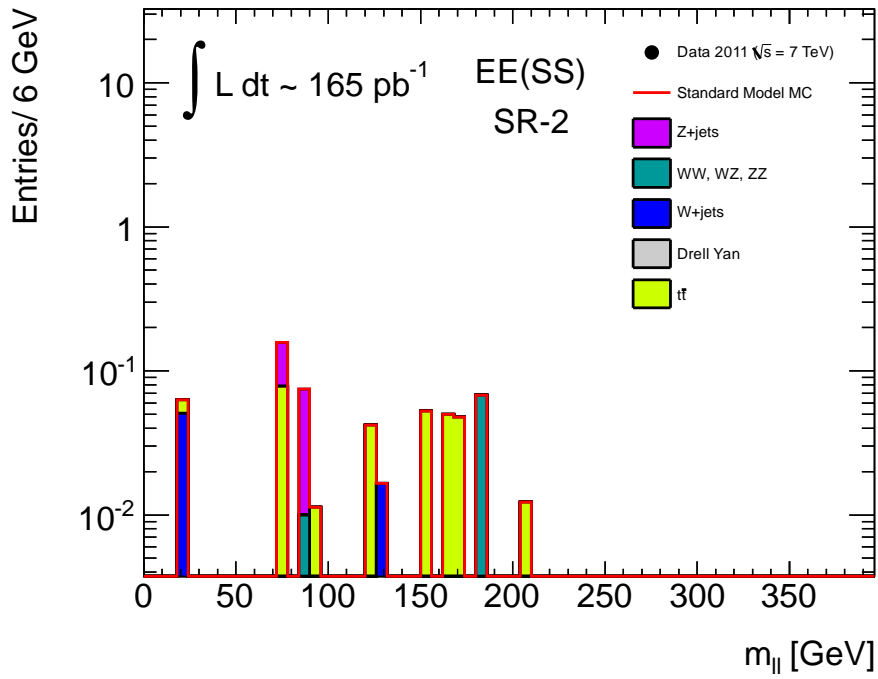


Figure 6.14: Invariant mass distribution in SS SR-2

Bin [GeV]	N(TT)	N(IT)	N(II)	f	r	N(RR)	N(RF)	N(FF)
0-30	1	10	13	0.173	0.848	-0.6	1.0	0.5
30-60	0	7	13	0.173	0.848	-0.97	0.4	0.6
60-90	0	4	0	0.173	0.848	-0.9	0.9	0.0
90-120	0	2	1	0.173	0.848	-0.4	0.4	0.0
120-150	0	0	0	0.173	0.848	0	0	0
150-180	0	0	0	0.173	0.848	0	0	0
180-210	0	0	0	0.173	0.848	0	0	0
210-240	0	0	0	0.173	0.848	0	0	0
240-270	0	0	0	0.173	0.848	0	0	0
Overflow	0	0	0	0.173	0.848	0	0	0

Table 6.6: Binwise fake/real estimation for  $E_T^{miss}$  distribution in SS channel with  $N_{jet} \geq 2$  requirement

## 6.8 Discussion

For the 2011 analysis presented, it is obvious from the invariant mass distributions in the individual signal regions, that in each of the three signal regions OS SR-1, OS SR-2 and SS SR-1 there is one data point present. This point is estimated to be a real-real event when comparing it with the estimated numbers in the corresponding tables.

For the estimation so far done with only  $165 \text{ pb}^{-1}$ , we can conclude that the fake contribution in the signal region is rather negligible. All present data points are estimated as real-real events.

Although the method provided a good estimation for the QCD contribution, there are some things one might consider to improve in order to make the predictions more accurate.

A best suited fake control region was selected but still it bore some deficiencies. Obviously the purity for exclusively loose - tight pairs was very low due to a significant contribution from tight electrons. One might consider to widen the Z-veto from 5 GeV to 10 GeV in order to remove more electrons coming from weak processes, which would raise the purity. Yet statistics is a limiting factor in this analysis — control regions showing satisfying purities often suffer from a lack of statistics. With more data included into the analysis, the statistical problem could certainly be eased. Another way to make the method more precise might be to keep the original 4-by-4 matrix (5.6). In the current work, electrons were not distinguished so the matrix was finally reduced to a 3-by-3 matrix which constitutes simplification.



## 7. Summary

With the first data taken in 2011 (corresponding to  $165 \text{ pb}^{-1}$ ), a data-driven background estimation for the QCD component in SUSY searches in the dilepton channel was developed using the matrix method. This background can only be hardly modelled with MC.

The principle of the matrix method relies on the definition of two samples of identification criteria for electrons, namely loose and tight. The aim of the analysis was to give an estimation on how many of dielectron events that pass all selection cuts are originating from QCD processes.

This was done by calculating the probability that fake preselected electrons pass tight criteria as well as the probability that real preselected electrons pass tight criteria. To determine these probabilities (i.e. efficiencies) one has to make use of control regions which are either dominated by fake electrons or by real electrons. The big challenge in defining fake control regions is to choose a QCD dominated region that has a similar composition as the fake composition in the signal region of the dilepton channel. In the analysis presented several control regions were investigated in order to suppress mainly weak background coming from  $Z$  decay processes. Particularly fake efficiencies can be very sensitive to the selection of appropriate control regions.

The final choice of control regions mainly relies on statistics and purity of the sample. The latter does not go into the calculation but evaluating the purity of control samples, helps to select the one which is best suited for the final estimation — the aim is to work with a fake control region contaminated as little as possible by other SM processes.

The QCD contribution has been successfully estimated using the matrix method for both 2010 (see Appendix) and 2011 data. The contribution from fake electrons in the signal regions is shown to be negligible.

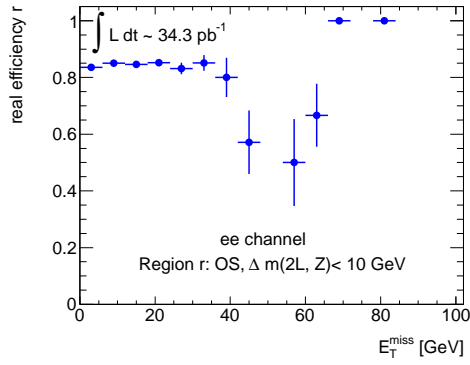
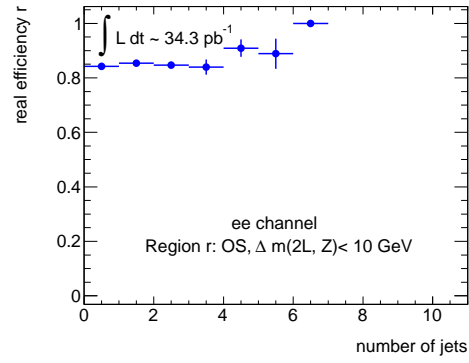




# A. Results from QCD Background Estimation with 2010 Data

This additional chapter is only intended to give an overview on the results for the QCD background estimation obtained by applying the matrix method to 2010 data. The data corresponds to an integrated luminosity of  $34.3 \text{ pb}^{-1}$ . Old object definitions and event selection from 2010 used here are described in [18]. For a detailed presentation and discussion of the method applied see chapter 5 and 6.

## A.1 Real Efficiencies

(a) real efficiency vs  $E_T^{miss}$ 

(b) real efficiency vs jet multiplicity

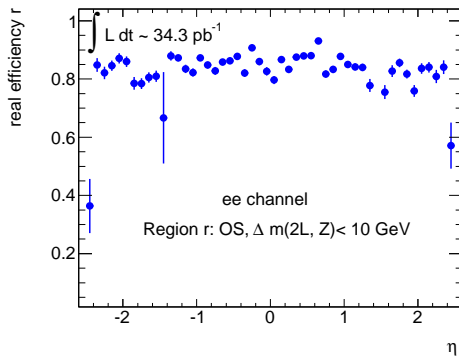
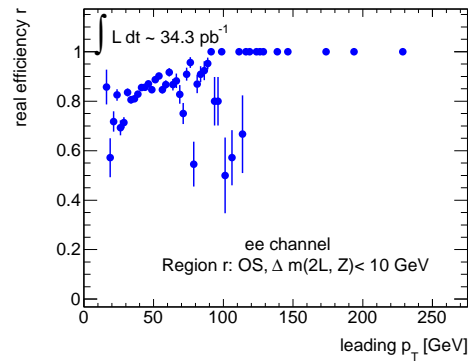
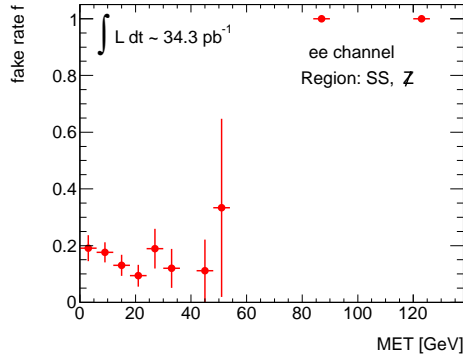
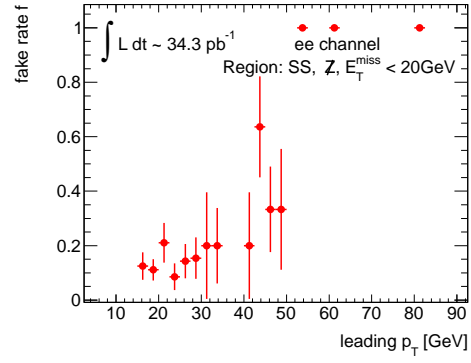
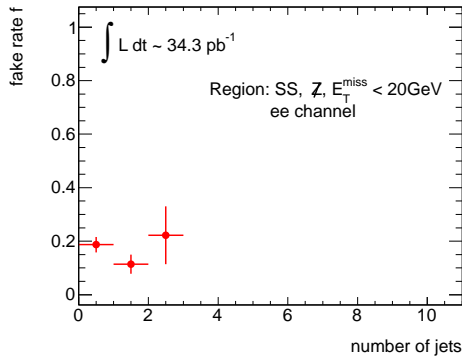
(c) real efficiency vs  $\eta$ (d) real efficiency vs leading  $p_T$ 

Figure A.1: Real efficiency extracted from the real electron control region (OS,  $\Delta m(l, Z) < 10$  GeV) plotted as a function of different event variables. The average value obtained is  $r = 0.843$ .

## A.2 Fake Rates

(a) fake-rate vs  $E_T^{miss}$ (b) fake-rate vs leading electron  $p_T$ 

(c) fake-rate vs jet multiplicity

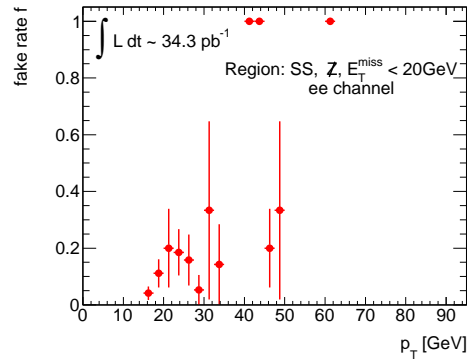
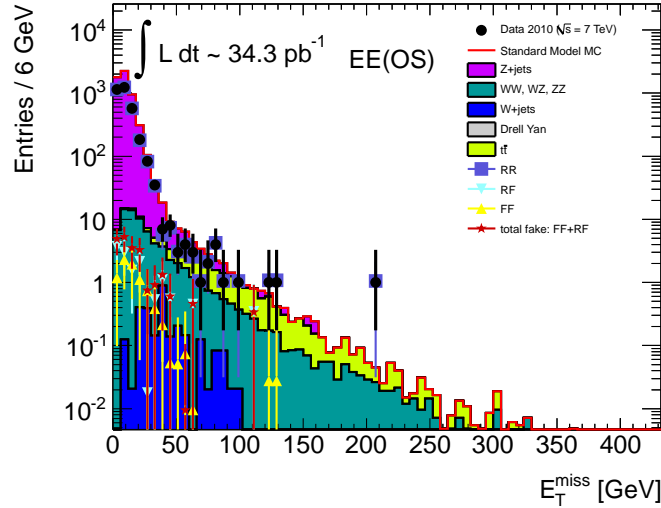
(d) fake-rate vs (both)  $p_T$ 

Figure A.2: Electron fake rates from the selected QCD control region (SS,  $E_T^{miss} < 20 \text{ GeV}$ , Z) plotted as a function of different event variables. The average value obtained is  $f = 0.147$ .  $E_T^{miss}$  distribution has no cut on  $E_T^{miss}$ .

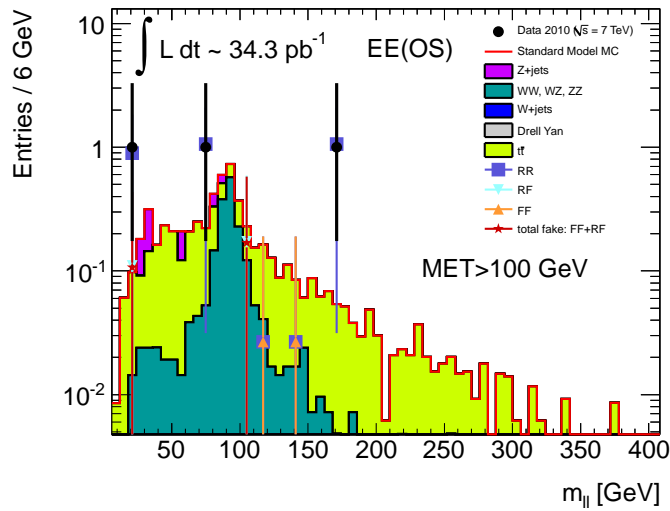
## A.3 Results

### A.3.1 OS SR

The signal region for the OS dielectron channel is in 2010 analysis defined by  $E_T^{miss} > 100$  GeV. As can be seen in figure A.3(b) showing an invariant mass distribution and from table A.1, all 3 data points present are estimated as real-real events.



(a) Dielectron OS  $E_T^{miss}$  distribution including fake estimation



(b) Invariant mass distribution including fake estimation in OS SR

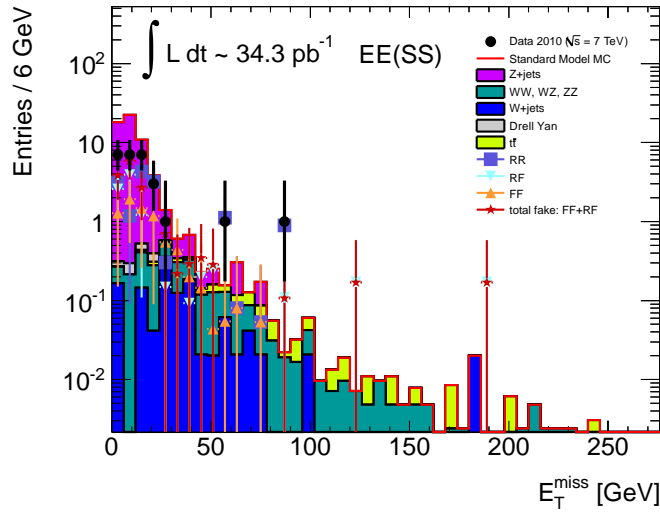
Figure A.3: Dielectron OS final states including fake estimation

Bin [GeV]	N(TT)	N(IT)	N(II)	f	r	N(RR)	N(RF)	N(FF)
0-30	3136	1312	380	0.147	0.843	3119	10.5	6.5
30-60	136	81	64	0.147	0.843	132.5	2.1	1.4
60-90	14	6	4	0.147	0.843	14.0	-0.1	0.1
90-120	2	2	0	0.147	0.843	1.8	0.2	0
120-150	2	0	2	0.147	0.843	2.2	-0.2	0.1
150-180	0	0	0	0.147	0.843	0	0	0
180-210	0	0	0	0.147	0.843	0	0	0
210-240	1	0	0	0.147	0.843	1.1	-0.1	0.0
240-270	0	0	0	0.147	0.843	0	0	0
Overflow	0	0	0	0.147	0.843	0	0	0

Table A.1: Binwise fake/real estimation for  $E_T^{miss}$  distribution in OS channel

### A.3.2 SS SR

In the SS signal region defined by  $E_T^{miss} > 80$  GeV no data points can be found in the signal region as can be seen in figure A.4(a) and from table A.2.



(a)

Figure A.4: Dielectron SS  $E_T^{miss}$  distribution including fake estimation

Bin [GeV]	N(TT)	N(IT)	N(II)	f	r	N(RR)	N(RF)	N(FF)
0-30	24	119	240	0.147	0.843	11.9	6.3	5.9
30-60	1	20	55	0.147	0.843	-0.8	0.5	1.4
60-90	1	0	7	0.147	0.843	1.2	-0.4	0.2
90-120	0	0	0	0.147	0.843	0.0	0.0	0.0
120-150	0	1	0	0.147	0.843	-0.2	0.2	0.0
150-180	0	0	0	0.147	0.843	0	0	0.0
180-210	0	1	0	0.147	0.843	-0.2	0.2	0.0
210-240	0	0	0	0.147	0.843	0	0	0
240-270	0	0	0	0.147	0.843	0	0	0
Overflow	0	0	0	0.147	0.843	0	0	0

Table A.2: Binwise fake/real estimation for  $E_T^{miss}$  distribution in SS channel

# B. Monte Carlo Samples

The Monte Carlo samples used for 2011 analysis are listed her with sample ID, generator, cross section and k-factor numbers.

## B.1 W+Jets

Sample ID	Name	Generator	$\sigma \times \text{BR}$ [pb]	k-factor
107680	WenuNp0_pt20	AlpgenJimmy	$6.9 \cdot 10^3$	1.20
107681	WenuNp1_pt20	AlpgenJimmy	$1.3 \cdot 10^3$	1.20
107682	WenuNp2_pt20	AlpgenJimmy	$3.8 \cdot 10^2$	1.20
107683	WenuNp3_pt20	AlpgenJimmy	$1.0 \cdot 10^2$	1.20
107684	WenuNp4_pt20	AlpgenJimmy	$2.5 \cdot 10^1$	1.20
107685	WenuNp5_pt20	AlpgenJimmy	6.9	1.20
107690	WmunuNp0_pt20	AlpgenJimmy	$6.9 \cdot 10^3$	1.20
107691	WmunuNp1_pt20	AlpgenJimmy	$1.3 \cdot 10^3$	1.20
107692	WmunuNp2_pt20	AlpgenJimmy	$3.8 \cdot 10^2$	1.20
107693	WmunuNp3_pt20	AlpgenJimmy	$1.0 \cdot 10^2$	1.20
107694	WmunuNp4_pt20	AlpgenJimmy	$2.5 \cdot 10^1$	1.20
107695	WmunuNp5_pt20	AlpgenJimmy	6.9	1.20
107700	WtaunuNp0_pt20	AlpgenJimmy	$6.9 \cdot 10^3$	1.20
107701	WtaunuNp1_pt20	AlpgenJimmy	$1.3 \cdot 10^3$	1.20
107702	WtaunuNp2_pt20	AlpgenJimmy	$3.8 \cdot 10^2$	1.20
107703	WtaunuNp3_pt20	AlpgenJimmy	$1.0 \cdot 10^2$	1.20
107704	WtaunuNp4_pt20	AlpgenJimmy	$2.5 \cdot 10^1$	1.20
107705	WtaunuNp5_pt20	AlpgenJimmy	6.9	1.20

## B.2 Z+Jets

Sample ID	Name	Generator	$\sigma \times \text{BR}$ [pb]	k-factor
107650	ZeeNp0_pt20	AlpgenJimmy	$6.6 \cdot 10^2$	1.25
107651	ZeeNp1_pt20	AlpgenJimmy	$1.3 \cdot 10^2$	1.25
107652	ZeeNp2_pt20	AlpgenJimmy	$4.0 \cdot 10^1$	1.25
107653	ZeeNp3_pt20	AlpgenJimmy	$1.1 \cdot 10^1$	1.25
107654	ZeeNp4_pt20	AlpgenJimmy	2.9	1.25
107655	ZeeNp5_pt20	AlpgenJimmy	$7.5 \cdot 10^{-1}$	1.25
107660	ZmumuNp0_pt20	AlpgenJimmy	$6.6 \cdot 10^2$	1.25
107661	ZmumuNp1_pt20	AlpgenJimmy	$1.3 \cdot 10^2$	1.25
107662	ZmumuNp2_pt20	AlpgenJimmy	$4.0 \cdot 10^1$	1.25
107663	ZmumuNp3_pt20	AlpgenJimmy	$1.1 \cdot 10^1$	1.25
107664	ZmumuNp4_pt20	AlpgenJimmy	2.9	1.25
107665	ZmumuNp5_pt20	AlpgenJimmy	$7.5 \cdot 10^{-1}$	1.25
107670	ZtautauNp0_pt20	AlpgenJimmy	$6.6 \cdot 10^2$	1.25
107671	ZtautauNp1_pt20	AlpgenJimmy	$1.3 \cdot 10^2$	1.25
107672	ZtautauNp2_pt20	AlpgenJimmy	$4.0 \cdot 10^1$	1.25
107673	ZtautauNp3_pt20	AlpgenJimmy	$1.1 \cdot 10^1$	1.25
107674	ZtautauNp4_pt20	AlpgenJimmy	2.9	1.25
107675	ZtautauNp5_pt20	AlpgenJimmy	$7.5 \cdot 10^{-1}$	1.25

## B.3 $t\bar{t}$

Sample ID	Name	Generator	$\sigma \times \text{BR}$ [pb]	k-factor
105200	T1	MC@NLO Jimmy	$8.9 \cdot 10^1$	-

## B.4 QCD

Sample ID	Name	Generator	$\sigma \times \text{BR}$ [pb]	k-factor
108326	$b\bar{b}_e$ _filter	PythiaB	$75.1 \cdot 10^3$	-

## B.5 Diboson

Sample ID	Name	Generator	$\sigma \times \text{BR}$ [pb]	k-factor
105985	WW	Herwig	$1.7 \cdot 10^1$	-
105986	ZZ	Herwig	$1.3 \cdot 10^1$	-
105987	WZ	Herwig	$5.5 \cdot 10^1$	-



## B.6 Drell Yan

Sample ID	Name	Generator	$\sigma \times \text{BR}$ [pb]	k-factor
116250	ZeeNp0_Mll10to40	AlpGenJimmy	$3.0 \cdot 10^3$	-
116251	ZeeNp1_Mll10to40	AlpGenJimmy	84.91	-
116252	ZeeNp2_Mll10to40	AlpGenJimmy	41.19	-
116253	ZeeNp3_Mll10to40	AlpGenJimmy	8.35	-
116254	ZeeNp4_Mll10to40	AlpGenJimmy	1.85	-
116255	ZeeNp5_Mll10to40	AlpGenJimmy	0.46	-
116260	Z $\mu\mu$ Np0_Mll10to40	AlpGenJimmy	$3.0 \cdot 10^3$	-
116261	Z $\mu\mu$ Np1_Mll10to40	AlpGenJimmy	84.78	-
116262	Z $\mu\mu$ Np2_Mll10to40	AlpGenJimmy	41.13	-
116263	Z $\mu\mu$ Np3_Mll10to40	AlpGenJimmy	8.34	-
116264	Z $\mu\mu$ Np4_Mll10to40	AlpGenJimmy	1.87	-
116265	Z $\mu\mu$ Np5_Mll10to40	AlpGenJimmy	0.46	-
116270	Z $\tau\tau$ Np0_Mll10to40	AlpGenJimmy	$3.0 \cdot 10^3$	-
116271	Z $\tau\tau$ Np1_Mll10to40	AlpGenJimmy	84.88	-
116272	Z $\tau\tau$ Np2_Mll10to40	AlpGenJimmy	41.28	-
116273	Z $\tau\tau$ Np3_Mll10to40	AlpGenJimmy	8.35	-
116274	Z $\tau\tau$ Np4_Mll10to40	AlpGenJimmy	1.83	-
116275	Z $\tau\tau$ Np5_Mll10to40	AlpGenJimmy	0.46	-



# Bibliography

- [1] GRIFFITHS, David: *Introduction to Elementary Particles*. John Wiley & Sons Inc, 1987
- [2] PERKINS, Donald H.: *Introduction to High Energy Physics*. Addison-Wesley Publishing Company, Inc., Third Edition, 1987
- [3] BIEBEL, Otmar: *Standardmodell der Teilchenphysik und Erweiterungen*. Lecture notes, SS 2009
- [4] WEBBER, Bryan R.: Fragmentation and Hadronization. In: *Proceedings of the XIX International Symposium on Lepton and Photon Interactions at High Energies*. Stanford, California, USA, August 1999. – <http://www.slac.stanford.edu/econf/C990809/docs/webber.pdf>
- [5] RUBBIA, Carlo: *Experimental Observation of the Intermediate Vector Bosons  $W^+$ ,  $W^-$  and  $Z^0$* . Nobel Lectures, Physics 1981-1990, 1984. – [http://nobelprize.org/nobel\\_prizes/physics/laureates/1984/rubbia-lecture.pdf](http://nobelprize.org/nobel_prizes/physics/laureates/1984/rubbia-lecture.pdf)
- [6] MARTIN, Stephen P.: A Supersymmetry Primer. In: *arXiv:hep-ph/9709356* (2008), Dezember
- [7] KANE, Gordon ; PIERCE, Aaron: *Perspectives on LHC Physics*. World Scientific Publishing Co. Pte. Ltd., 2008
- [8] PUBLIC CERN WEB PAGE: *The Large Hadron Collider*. <http://public.web.cern.ch/public/en/LHC/LHC-en.html>, Juni 2011
- [9] *LHC Machine Outreach*. <http://lhc-machine-outreach.web.cern.ch>, Juni 2011
- [10] PUBLIC CERN WEB PAGE: *The accelerator complex*. <http://public.web.cern.ch/public/en/Research/AccelComplex-en.html>, Juni 2011
- [11] US/LHC: *The science of LHCf*. [http://www.uslhc.us/LHC\\_Science/Experiments/LHCf](http://www.uslhc.us/LHC_Science/Experiments/LHCf), Juni 2011
- [12] THE ATLAS COLLABORATION: *WorkBook - The ATLAS Experiment*. <https://twiki.cern.ch/twiki/bin/viewauth/Atlas/WorkBookAtlasExperiment>, Juni 2011
- [13] *ATLAS experiment - etour*. [http://www.atlas.ch/etours\\_exper](http://www.atlas.ch/etours_exper), Juni 2011
- [14] THE ATLAS COLLABORATION: *The ATLAS detectors*. <https://twiki.cern.ch/twiki/bin/viewauth/Atlas/AtlasDetectors>, Juni 2011

- [15] THE ATLAS COLLABORATION: The ATLAS Experiment at the CERN Large Hadron Collider. (2008), August. – JINST 3 S08003
- [16] THE GERMAN ATLAS GROUP: *ATLAS Requirements for the National Analysis Facility*. [naf.desy.de/sites/site\\_naf/content/e145/e194/A-NAF.pdf](http://naf.desy.de/sites/site_naf/content/e145/e194/A-NAF.pdf), 2007
- [17] GLADYSHEV, A. V. ; KAZAKOV, D. I.: Supersymmetry and LHC. In: *arXiv:hep-ph/0606288v1* (2006), June 28,
- [18] THE ATLAS COLLABORATION: SUSY searches with dileptons and high missing transverse momentum. In: *ATL-PHYS-INT-2011-030* (2011)
- [19] THE ATLAS COLLABORATION: Expected electron performance in the ATLAS experiment. In: *ATL-PHYS-INT-2010-126* (2010)
- [20] THE ATLAS COLLABORATION: *ATLAS EGamma group - Electron Reconstruction*. <https://twiki.cern.ch/twiki/bin/view/AtlasProtected/ElectronReconstruction>, Juli 2011
- [21] THE ATLAS COLLABORATION: *ATLAS EGamma group - Electron Identification*. <https://twiki.cern.ch/twiki/bin/view/AtlasProtected/ElectronIdentification>, Juli 2011
- [22] THE ATLAS COLLABORATION: *Electrons and Photons*. <http://cdsweb.cern.ch/record/1159567/files/Electrons%20and%20Photons%20%28p43%29.pdf>, Dezember 2008. – CSC chapter on electrons, "Reconstruction and Identification of Electrons"
- [23] THE ATLAS COLLABORATION: Expected performance of the ATLAS experiment. In: *CERN-OPEN-2008-020* (2008)
- [24] THE ATLAS COLLABORATION: Performance of Jet Algorithms in the ATLAS Detector. In: *ATL-COM-PHYS-2009-630* (2009)
- [25] THE ATLAS COLLABORATION: *PileupReweighting*. <https://twiki.cern.ch/twiki/bin/view/AtlasProtected/PileupReweighting>, Juli 2011
- [26] THE ATLAS COLLABORATION: *Calculation of MET*. <https://svnweb.cern.ch/trac/atlasoff/browser/PhysicsAnalysis/D3PDMaker/SUSYD3PDMaker/tags/SUSYD3PDMaker-00-10-15/python/SUSYCustomMET.py#L40>, Juli 2011
- [27] THE ATLAS COLLABORATION: Performance of the Missing Transverse Energy Reconstruction and Calibration in Proton-Proton Collisions at a Center-of-Mass Energy of  $\sqrt{s} = 7$  TeV with the ATLAS Detector. In: *ATLAS-CONF-2010-057* (2010)
- [28] THE ATLAS COLLABORATION: Reconstruction and Calibration of Missing Transverse Energy and Performance in Z and W events in ATLAS Proton-Proton Collisions at  $\sqrt{s} = 7$  TeV. In: *ATLAS note in preparation* (2011)
- [29] THE ATLAS COLLABORATION: Search for Supersymmetry with two leptons and missing transverse energy momentum at  $\sqrt{s} = 7$  TeV. In: *ATL-COM-PHYS-2011-649*. – ATLAS Internal note in preparation

- 
- [30] THE ATLAS COLLABORATION: Background studies for top-pair production in lepton plus jets final states in  $\sqrt{s} = 7$  TeV ATLAS data. In: *ATLAS-CONF-2010-087* (2010)
- [31] ARNOWITT, Richard ; NATH, Pran: *Advanced Series on Directions in High Energy Physics*. Bd. 21: *Developments in Supergravity Unified Models*. 2010
- [32] GLASHOW, Sheldon L.: Partial-symmetries of weak interaction.
- [33] GLASHOW, S. L.: Partial Symmetries of Weak Interactions. In: *Nucl. Phys.* 22 (1961). [http://dx.doi.org/10.1016/0029-5582\(61\)90469-2](http://dx.doi.org/10.1016/0029-5582(61)90469-2). – DOI 10.1016/0029-5582(61)90469-2
- [34] THE ATLAS COLLABORATION: *The ATLAS Computing Workbook*. <https://twiki.cern.ch/twiki/bin/viewauth/Atlas/WorkBook>, Juni 2011



# Acknowledgments

An dieser Stelle möchte ich mich bei allen bedanken, die zu dieser Arbeit beigetragen haben.

- Mein erste Dank gilt Prof. Dr. Dorothee Schaile, die mich an diesem Lehrstuhl aufgenommen und mir die Möglichkeit gegeben hat, diese Diplomarbeit anzufertigen.
- Ich bedanke mich bei Prof. Dr. Jochen Schieck für die Übernahme des Zweitgutachtens.
- Ein ganz besonderer Dank gilt Dr. Federica Legger für die ausgezeichnete Betreuung während des letzten Jahres, für alle Hilfestellungen und nicht zuletzt für das Korrekturlesen dieser Arbeit. Molte grazie!
- Insgesamt möchte ich mich bei allen nicht namentlich erwähnten Mitgliedern dieses Lehrstuhls für ein nettes, offenes und sehr hilfsbereites Arbeitsklima bedanken!
- Insbesondere bedanke ich mich bei meiner Bürokollegin Josephine Wittkowski für die vielen netten und lustigen Gespräche während des letzten Jahres. Weiterhin gilt mein Dank Stefanie Adomeit, Alexander Ruschke und Julien de Graat für eine schöne Zeit am Lehrstuhl, sowie für diverse Unternehmungen auch außerhalb der Physik.
- Ich bedanke mich bei Frau Franz, die stets eine große Hilfe bei administrativen Fragen aller Art war.
- Ein weiterer Dank gilt meinen Studienkollegen Sarah Schulz und Leonhard Neuhaus für tolle vergangene 5 Jahre, auch wenn sich die Wege mittlerweile getrennt haben.
- Ich danke weiterhin Anna Fritscher für sehr viel und hoffentlich viele weitere schöne Jahre.
- Ich danke meinem Bruder Nemanja Vujaklija (nicht zuletzt auch für das teilweise Korrekturlesen dieser Arbeit).

Zuletzt möchte ich mich ganz besonders bei meinen Eltern bedanken, die mich immer bedingungslos unterstützt und mir das Studium der Physik ermöglicht haben.





## **Erklärung**

Hiermit versichere ich, dass ich die vorliegende Arbeit selbstständig verfasst und keine anderen als die angegebenen Quellen und Hilfsmittel benutzt habe, dass alle Stellen der Arbeit, die wörtlich oder sinngemäß aus anderen Quellen übernommen wurden, als solche kenntlich gemacht sind und dass die Arbeit in gleicher oder ähnlicher Form noch keiner Prüfungsbehörde vorgelegt wurde.

München, 19. Juli 2011